Mass Spectrometry Imaging of the Subchondral Bone in Osteoarthritis Reveals Tissue Remodeling of Extracellular Matrix Proteins that Precede Cartilage Loss

Charles A. Schurman[1], Joanna Bons[1], Jonathon J. Woo[2], Cristal Yee[2], Nannan Tao[3], Tamara Alliston[2], Peggi M. Angel[4], Birgit Schilling[1]

[1] Buck Institute for Research on Aging, 8001 Redwood Blvd, Novato, CA, 94945, USA

[2] Department of Orthopaedic Surgery, University of California San Francisco, 35 Medical Center Way, San Francisco, CA 94143, USA,

[3] Bruker Daltonics Inc, 101 Daggett Dr. San Jose, CA, 95134, USA

[4] Department of Pharmacology & Immunology, Medical University of South Carolina, 173 Ashley Avenue, Charleston, SC 29425, USA

Corresponding Author:

Birgit Schilling, Ph.D.

Professor, Buck Institute for Research on Aging

Director, Mass Spectrometry and Proteomics Core

Buck Institute for Research on Aging

Novato, CA 94945, USA

bschilling@buckinstitute.org

Abstract

Osteoarthritis (OA) of the knee is a degenerative condition of the skeletal extracellular matrix (ECM) marked by the loss of articular cartilage and subchondral bone homeostasis. Treatments for OA in the knee beyond full joint replacement are lacking primarily due to gaps in molecular knowledge of the biological drivers of disease. Here, Mass Spectrometry Imaging (MSI) enabled molecular spatial mapping of the proteomic landscape of human knee tissues. Histologic sections of human tibial plateaus from OA patients and cadaveric controls were treated with collagenase III to target ECM proteins prior to imaging using a timsTOF fleX mass spectrometer (Bruker) for matrix-assisted laser desorption ionization (MALDI)-MSI of bone and cartilage proteins in human knees. Spatial MSI data of the knee, using sections of the tibial plateau from non-arthritic, cadaveric donors or from knee replacement patients with medial OA were processed and automatically segmented identifying distinct areas of joint damage. ECM peptide markers compared either OA to cadaveric tissues or OA medial to OA lateral. Not only did candidate peptides distinguish OA relative to intact cartilage, but also emphasized a significant spatial difference between OA and intact subchondral bone (AUROC >0.85). Overall, 31 peptide candidates from ECM proteins, including COL1A1, COL3A1, and unanticipated detection of collagens COL6A1 and COL6A3 in adult bone, exhibited significantly elevated abundance in diseased tissue. Highly specific hydroxyproline-containing collagens dominated OA subchondral bone directly under regions of lost cartilage revealing dramatic tissue remodeling providing molecular details on the progression of joint degeneration in OA. The identification of specific spatial markers for the progression of subchondral bone degeneration in OA advances our molecular understanding of coupled deterioration of joint tissues.

Introduction

Osteoarthritis (OA) is the most common joint disease worldwide with the prevalence of OA increasing with age such that around half of all women (48.1%) and nearly one third of men (31.2%) aged 65 years and over [1, 2] suffer from this debilitating joint disease. The future burden of musculoskeletal diseases is only expected to escalate in the coming decades as lifespans increase and more individuals become affected by comorbidities and other risk factors for OA, such as obesity, hypertension, dyslipidemia, dementia, and Alzheimer's Disease [3, 4]. Given that osteoarthritis and its risk factors all increase with age, we sought to understand more deeply the molecular changes, and specifically the spatial profile changes occurring in joint tissues in patients with clinically diagnosed OA and in non-arthritic individuals.

The relationship between subchondral bone and articular cartilage changes in OA, with progressive changes in subchondral bone remodeling, mineralization, vascularity, and innervation that parallel cartilage degeneration is well documented [5, 6]. In the early stages of OA, subchondral bone undergoes increased bone resorption, but at later stages, deregulated bone remodeling leads to increased subchondral bone density [5-7]. In addition to thickening of the subchondral bone plate, OA is often accompanied by microarchitectural changes in trabecular bone and bone marrow lesions [8, 9]. Indeed, clinical magnetic resonance imaging (MRI) identifies early changes to subchondral bone as predictors of later stage joint pain and joint replacement, even before detectable changes in the overlying cartilage [10]. These observations motivate the search for diagnostics or interventions targeting subchondral bone to detect and retard OA progression, prior to the loss of articular cartilage, while the disease may still be reversible [11]. However, many questions remain about the cellular and molecular targets for such interventions. Multiple cell types, including osteoblasts, osteoclasts, osteocytes, mesenchymal progenitors, and others, have been implicated in the subchondral bone changes in OA. In addition, aging, OA, and diseases such as type II diabetes cause changes in collagen post-translational modifications, including prolyl hydroxylation, glycation, and others [12, 13]tied to alterations in bone matrix material properties [14, 15]. In order to understand the loss of subchondral bone and cartilage homeostasis in OA, an unbiased spatial analysis of the proteomic changes in each component of the multi-tissue joint environment is needed. Unfortunately, the complex nature of the ECM of bone and cartilage tissues clearly requires further studies has long obstructed proteomic profiling and molecular characterization that has been successfully applied in many other tissues.

Matrix-Assisted Laser Desorption/Ionization - Mass Spectrometry Imaging (MALDI-MSI) is a rapidly advancing technology that allows for the direct detection of analytes in their spatial location directly from tissue sections. Initially developed in the 1990s, MALDI-MSI has been instrumental in pathology research by providing an alternative to traditional histopathologic and immunocytochemical

stains by directly imaging target proteins [16, 17]. Since its inception, MALDI-MSI has been used in dozens of disease and tissue contexts including studies on neurodegenerative diseases and cancers, among others [18-21], and has expanded from peptide-based imaging to include small molecule analytes such as lipids, metabolites, and even large macromolecular glycan structures [22-24]. The application of MALDI-MSI in the field of biomedical research, along with other mass spectrometry imaging technologies such water-assisted laser desorption ionization (SpiderMass) [25], has opened new frontiers by enabling the identification of possible new diagnostic compounds or biomarkers in place in their direct biological context [26].

In previous years, investigators have begun to utilize MALDI-MSI to investigate the molecular landscape of OA, but with more focus on lipids and glycans in cartilage and synovial tissues [27-29]. Recently, MALDI-MSI has been employed to investigate the lipid profiles and their distributions in the synovial membrane and infrapatellar fat pad of human OA patients revealing the importance of lipid species in the development and regulation of inflammatory processes in OA, while others have extended these lipid and metabolite analyses to articular cartilage [30-32]. Recently, spatial profiling of the subchondral bone has been achieved for lipids, expanding MALDI-MSI to mineralized tissues [33-36]. Other investigators have utilized MALDI-MSI to study N-glycans in the subchondral bone of the knee in OA and identify specific glycans within subchondral trabecular bone that are upregulated in different joint quadrants that may correspond to areas of altered mechanical loading with disease [29, 37, 38]. While these studies represent advancements in the use of MALDI-MSI overall in subchondral bone, protein imaging of joint tissues has thus far been limited to the synovium and articular cartilage in human and equine samples and not yet bone tissue [29, 39, 40]. The highly complex secondary and tertiary structure and crosslinked nature of the bone ECM presents a technical hurdle in the application of protein-based MALDI-MSI techniques to the study of subchondral bone changes in OA. However, significant advancements utilizing collagenase III based enzymatic protein digestions have proved potent in the study of other ECM dense tissues and diseases such as breast, lung, and prostate cancers as well as in infarcted cardiac tissues [20, 21, 41, 42]. Collagenase III, also known as matrix metalloproteinase-13 (MMP-13), is a potent proteinase with a broad spectrum of activity against various ECM proteins, including collagen types I, II, and III. Homeostatically, this enzyme is involved in the degradation and turnover of the ECM, essential in processes such as bone formation and remodeling, rendering it the ideal enzymatic choice to prepare bone and joint tissues for protein-based MALDI-MSI.

In this report, we spatially investigate the extracellular protein content and ECM remodeling of human end-stage OA of the knee, demonstrating the first use of a collagenase III on-slide enzymatic digestion for formalin fixed paraffin embedded (FFPE) knee joint tissues from OA patients (N=4) and non-arthritic cadaveric, age-matched control donors (N=4) for protein-based MALDI-MSI **(Figure 1)**.

In addition, these samples were prepared for serial glycan and ECM protein imaging [43, 44], demonstrating our optimized ability to complete multi-omics imaging on the same slides of human joint tissue composed of both bone and cartilage regions. This novel serial enzyme strategy allows for the visualization and classification of differences in ECM protein composition in OA and in healthy aging, including differences in post-translational modifications. Through identification of disease-regulated ECM proteins in OA, molecular mechanisms aggravating disease progression, potentially originating in the subchondral bone, may be spatially visualized for the first time to provide much needed novel disease markers that may be utilized to track, or even predict, osteoarthritis in humans.

Results

Human OA Cohort Specimen

This study analyzed spatial molecular proteomic changes in osteoarthritis (OA) of the medial tibial plateau of the knee, specifically the subchondral bone regions of affected knee joints using mass spectrometry imaging (MSI). First, four tibial plateaus from a group of non-OA diagnosed donors (cadaveric controls C1-C4) without history of osteonecrosis, osteoporosis, or fractures were collected through the Willed Body Program at the University of California, San Francisco. Second, four osteoarthritic tibial plateaus were collected as surgical discard from patients receiving total knee arthroplasty/replacement (Patients P1-P4), who were clinically diagnosed with stage IV Osteoarthritis of the medial tibial plateau of the knee **(Figure 1A)**. Recruitment occurred through referral from orthopedic surgeons at the Department of Veterans Affairs Medical Center (San Francisco, CA, USA). This resulted in an age, sex, and BMI matched cohort of human tibial plateaus that were stratified by their Osteoarthritis Research Society International (OARSI) score as graded by clinical pathologists as determined from histopathologic Safranin-O/Fast Green stains **(Supplemental Figures 1** and **2, Supplemental Table 1)**. Tibial plateaus, composed of the articular cartilage and underlying subchondral trabecular bone, were subsequently further divided into the medial and lateral halves to accommodate placement on standard 25x75 mm microscopy slides. This allowed for the comparison of medial OA sections (P1-P4, medial) to two distinct sets of ‘control’ tissues composed of i) tissue-matched OA lateral tibial plateau halves (from the same OA patients, P1-P4, lateral), and ii) site-matched non-arthritic cadaveric controls (C1-C4, medial) **(Figure 1B).**

Tissue Preparation for Spatial Molecular Imaging of Extracellular Matrix (ECM) in OA Joints

While Matrix-Assisted Laser Desorption Ionization – Mass Spectrometry Imaging (MALDI-MSI) workflows have been applied to many tissue types, molecular imaging via MALDI-MSI of subchondral bone from joint tissues on the protein level has not been reported so far, as it requires specific optimized conditions to maintain tissue integrity on the imaging slides. Formalin fixed, paraffin

embedded human tibial plateau tissue slides were prepared for enzymatic digestion using previously published protocols [23, 43, 45, 46] **(Figure 1C)** with important modifications in consideration of the large, ECM-rich tissue sections of the human tibial plateaus. Notably, heat induced epitope retrieval steps were optimized to ensure survival of both cartilage and delicate subchondral trabecular bone. Tissue slides were first treated with PNGase F to process N-linked glycans for imaging and to increase the effectiveness of later proteolytic digestion **(Supplemental Figure 3)**. Even though our main emphasis was on the ECM protein imaging we did acquire the glycan MALDI MSI datasets as the workflow made this possible. Briefly, glycan imaging identified 46 glycan species from a database of 165 known glycan species in FFPE sections of intact human tibial plateaus from a subset of 3 OA patients **(Supplemental Table 2).** Comparing the lateral and medial halves of the three imaged patients (OA patients 2,3,4), some interesting spatial patterns were observed, such as a tendency for glycan signal to change in areas of subchondral bone damage in OA tissues, but significantly regulated glycans in OA were not yet detected, though other studies that have used large cohorts leveraging tissue microarrays do discriminate glycan changes in subchondral bone [37, 38]. Some glycans with preferential abundance for cartilage or bone regions were observed, but these did not appear to be disease regulated. Given our primary focus on ECM protein MS Imaging in this study, deciphering distinct glycan patterns in OA will require additional work in the future **(Supplemental Figure 3).**

Overall, glycan imaging and enzymatic glycan removal can be performed without impacting later serial enzymatic digestions for protein-based imaging. Specific care was taken to ensure that serial enzymatic digestion post glycan imaging would not disrupt the integrity of the tissue slide [43, 44]. Additional wash steps and epitope retrieval were meticulously optimized to ensure survival of the tibial plateaus through the multiple antigen retrieval and digestion steps. ECM-targeted enzymatic digestion for proteomic imaging was completed utilizing collagenase III that featured an enzymatic preference to cleave at repeated amino acid Gly-Xxx-Pro (GXP) motifs within the triple helical region of collagens [47, 48]. While preferably targeting collagens, this enzyme formulation also allowed for detection of several other ECM and ECM-related proteins **(Supplemental Table 3),** making it the ideal proteolytic enzymatic choice to investigate the degeneration of the skeletal ECM in both cartilage and bone in OA. MSI data was acquired with the timsTOF fleX (Bruker Scientific, LLC, Bremen, Germany) after complete slide preparation that included the ECM target enzymatic digestion and MALDI matrix application of alpha-cyano-4-hydroxycinnamic acid (CHCA). MSI generates spatial maps of the imaged tissue in which the intensities correspond to the abundance of a molecular feature (e.g., peptide) at the imaged location with a spot size of 20 μM, with variable step-size resolution from adjacent pixels at 20 μM laser step size to capture small regions in detail to a larger

step sizes of 120 μM or more to create images of the entire tissue section **(Figure 1D).** This molecular imaging technique allows for the acquisition of proteomic data in a spatial manner from both cartilage and bone, simultaneously offering spatially localized data on the degeneration of joint tissue.

MS Imaging and Spatial Proteomics of Skeletal Tissues in OA

Given the complexity of osteoarthritis, and the need for improved molecular markers for the disease, we sought to utilize MALDI-MSI to investigate changes to the ECM in both subchondral bone and cartilage. Here, we demonstrate the first spatial acquisition of proteomic MALDI-MSI data from composite knee joint tissues composed of both cartilage and bone regions. Given that protein level MALDI-MSI analysis of bone has not previously been reported, we first verified that the enzymatic approach using collagenase III could successfully provide relevant details about the skeletal ECM. From a representative non-arthritic, cadaveric control (individual 'C1'), 33,234 individual MS1 mass spectra, one for each imaged spot, across the entire tissue section were acquired at a 120 μm laser step size as an overview scan representing the entire tissue. The several thousand individual spectra were combined into a composite spectrum representative of the entire tissue **(Figure 2A)** with over 3,000 distinct individual peptide peaks each representing specific molecular features (peptides) with precise mass to charge (m/z) ratios. Individual peaks from the composite spectrum are identified and the corresponding m/z peak value for each pixel extracted and mapped back to the specific spatial location to generate heatmaps depicting its overall spatial distribution. For the tibial plateau, many strong peaks with good signal to noise ratios and clear peptidic isotope patterns were observed in the composite spectrum that featured spatial distributions found uniquely in the subchondral bone or the cartilage regions, respectively, while others emerged across both tissue types. Automated region segmentation **(Figure 2B)** was applied using the Segmentation algorithm within the SCiLS Lab software for the top 500 most intense peaks from the complex composite spectrum. This unbiased segmentation recognized regions of tissue that shared similar spectral profiles and grouped them together into regions. Hierarchical regions were created until areas resembling and surrounding the cartilage and bone tissues were generated, and the bone region divided until individual trabecula were able to be resolved from the marrow space. Although only operating on a subset of peaks from the full composite spectrum, this segmentation operation accurately captures 3 regions in non-arthritic, aged tissue **(Figure 2B)** that physiologically match i) the cartilage (blue), ii) the subchondral bone (orange), iii) and bone marrow (maroon) regions between trabecula; additional 'background' or pixels with little tissue specific signal (black) are also identified. The hierarchical segmentation tree

(Figure 2C) shows how many pixels are assigned into each of the generated regions based on their independent spectra.

To determine how well the automated segmentation corresponds to actual tissue type, we investigated whether known protein markers of bone and cartilage would be preferentially located in these automatically identified regions **(Figure 2D)**. Proteolytic peptides from COL1A1 and COL2A1, identified in studies of other tissue types [20, 41, 46, 49], were used as markers for bone and cartilage tissue within the non-arthritic sample (C1), respectively. The bone marker protein COL1A1 and its corresponding peptide $G^{317}PAGARGNDGATGAA^{331}$ with m/z at 1242.58, showed an intense signal predominantly in the orange 'subchondral bone' region (yellow outline, left), with almost no signal detected in the 'cartilage' region (yellow outline, right). Quantitatively, the pixel spots within the bone region had a significantly higher mean pixel intensity for the feature at m/z 1242.58 than the collection of pixels within the cartilage area by t-test ($p<0.0001$). Conversely, the cartilage marker protein COL2A1 and its peptide $G^{982}PQGLAGQR^{990}$ with m/z at 883.48, was most intensely abundant in the identified cartilage region with little to no signal intensity within the bone region. Compared via t-test, the automatically generated cartilage region also showed a significantly elevated mean pixel intensity ($p < 0.0001$) at this m/z compared to the bone regions. These automatically segmented tissue regions also match well to histopathology via Safranin-O / Fast Green stains on serial sections of the tissues **(Supplemental Figure 1).** To more clearly ascertain that MALDI-MSI will discern between bone and cartilage on the molecular level, a smaller region of the bone-cartilage junction was imaged at a higher spatial resolution using a laser step size of 20 µm **(Figure 2E)**, which is the step size matching the minimal laser ablation area. At this improved higher spatial resolution, it was evident that the signal from the COL1A1 peptide $G^{317}PAGARGNDGATGAA^{331}$ at m/z 1242.58 emerged uniquely from the trabecular bone. In contrast the peptide from COL2A1 $G^{982}PQGLAGQR^{990}$ with m/z 883.48 was detected specifically in the upper cartilage region. **Figure 2E** highlights the distinct spatial distribution of the latter bone and cartilage markers, and the two areas display distinct separation when visualized in a composite image. To solidify this finding, additional unique peptides from COL1A1 and COL2A1, $G^{626}PAGERGEQ^{634}$ with m/z at 900.40 and $G^{999}PSGEPGKQGAP^{1010}$ with m/z at 1097.63 respectively, were also compared across the bone and cartilage regions and showed similarly significant differences in mean pixel intensity between bone and cartilage areas (**Supplemental Figure 4A-B**) providing distinct spatial features that correlate to the tissue types. While these specific peptide markers illustrate almost a binary delineation between bone and cartilage tissue regions, other unexplored markers such as glycans or other ECM proteins may reveal even further granularity or gradients across the bone-cartilage junction.

Still, these higher resolution settings (20 μm laser step size) reveal exciting spatial distributions for multiple features discernable with individual bone trabecula – morphologic features that are themselves typically only at an average width of 200 μm. **Figure 2E** and **Supplemental Figure 4C** display a level of spatial detail and specificity superseding other traditional imaging techniques used within the skeleton. These spatial patterns reveal regions of high signal intensity specifically along the edges of trabecular bone for some m/z features, such as m/z at 1943.91, while others show the most intense signal in the innermost portions of trabecula, e.g. m/z at 1242.58 & m/z at 1406.71 (**Supplemental Figure 4C)**. These spatial differences, even below the microarchitectural (trabecular) level in bone, may give insight into the cellular dynamics of bone remodeling. MALDI-MSI identifies tissue type and tissue specific marker proteins even at sub-microarchitectural scales when applied to the extracellular matrix (ECM) of skeletal tissues.

Age-related Markers of Osteoarthritis – Using Medial Site-Matched Cadaveric Controls

Though some markers for cartilage degeneration can be detected in synovial fluid or in circulation, including small metabolites, lipids, inflammatory molecules, and by-products of proteoglycan and peptide catalysis [50], less is known about markers for bone degeneration. Since MALDI-MSI comprises the ability to accurately identify tissue type and tissue specific marker proteins in aged, non-arthritic bone and cartilage, we applied this technique to investigate the molecular landscape defining OA to uncover novel markers of disease. We first conducted a site-matched medial OA to medial Cadaveric comparison by comparing tissues from the most affected medial side of the joint in our OA patient cohort to the same region in age-matched non-arthritic cadaveric donor controls. Acquired MALDI-MSI data from joints of our representative control, C1, and the first OA patient, P1, **(Figure 3A)** were simultaneously loaded into the same SCiLS data processing workspace. This resulted in a combined data set of 59,084 individual spectra that were processed together as a single dataset. Automated region segmentation **(Figure 3B)** was performed for the top 500 most intense peaks from the combined dataset. Similar to the established segmentation processes for control tissue **(Figure 2)**, the automatically generated regions captured the cartilage regions and identified regions of non-arthritic

subchondral bone in both control cadaveric tissue and in the deeper trabecular bone of the OA patient. However, additional bone regions were identified in the most medial half of the tissue belonging to the OA patient P1 where cartilage has deteriorated, and arthritis damage would be most severe. The analysis identified a thin transitional layer of bone in between the diseased bone region in OA P1 and the area of bone in OA P1 that resembled healthier bone from donor C1.

To further investigate the differences between the identified diseased bone and the aged, non-arthritic bone, the two regions were isolated and new composite spectra generated using only the pixels from either region **(Figure 3C).** Many of the large prominent peaks in each spectrum show a change in intensity from the non-arthritic to the diseased regions signifying the dramatic molecular shift in bone during the course of OA. To determine which of the specific peaks are most different between the two bone regions, a Discriminating Feature analysis was performed that utilizes a receiver operating curve (ROC) to score individual features on how well spatial distributions match or predict the segmented region boundaries [51, 52]. Using a statistical threshold of an area under the receiver operating curve (AUC) of >0.85, 29 candidate features **(Supplemental Table 3)** were found when comparing the diseased region to the non-arthritic bone regions that best describe the differences between these two subclasses of trabecular bone. Spatial heat maps of the distribution of these 31 candidate markers in the medial side of representative patient P1 are shown in **Figure 3D.** To validate candidate features as potential osteoarthritis markers, we used the mean of feature (m/z) signal intensity from defined regions of tissue containing the diseased subchondral bone, which correlates to the abundance of the feature peptide at that location, as a quantitative metric to compare the larger OA cohort (n=4) to cadaveric controls (n=4) for each individual candidate feature from ROC analysis. To focus our analysis on the alterations to the bone in OA, we isolated the medial edge of all tissue sections where cartilage had deteriorated, and underlying bone damage would be the greatest. New ROIs were drawn encompassing the subchondral bone from the medial edge to the start of the remaining cartilage in OA samples, and from the medial edge to an equivalent region of bone underneath cartilage in control cadaveric samples **(Supplemental Figure 5A)**. Spectral data was then only exported for pixels within these ROIs to isolate diseased and non-arthritic bone and avoid the transitional bone subtype in OA samples. Finally, the mean pixel intensity was calculated for each candidate feature per tissue section. In a three-dimensional PLS-DA analysis **(Supplemental Figure 5 B)**, the cadaveric medial group separated from the medial OA samples when comparing by mean pixel intensity for the candidate features from ROC analysis. The average pixel intensity for each individual candidate feature was compared via Student's t-test between the site-matched cadaveric controls and the medial OA group to determine if there were robust differences across the patient cohort **(Figure 3E)**. Heatmaps for example candidate features with significant difference in abundance in OA with known peptide identifications are shown for an exemplary peptide of COL1A1 - $G^{626}PAGERGEQ^{634}$ with MH+ with m/z at 900.40, and for a post-translationally modified peptide of COL3A1 - $G^{471}EP^{(ox)}GAN^{(de)}GLP^{(ox)}GAAGERGAP^{(ox)488}$ with m/z at 1626.75 illustrating the increase of these features in the medial portions of OA tissues. Six of the 29 candidates, including peptides from COL1A1, COL1A2, FN1, and COL6A1, from this comparison reached significance in a student's t-test comparing OA samples against cadaveric controls with four biological replicates (N=4, $p < 0.05$), while

7 additional candidate features, including peptides for COL3A1 and several novel features that do not yet have peptide ID matches in existing databases, trended towards significant ($0.1<p<0.05$) with OA **(Supplemental Table 3)**.

Joint-site Specificity of Osteoarthritis: Comparison of Medial vs Lateral Joints in OA Patients

We identified promising peptide candidates with robust differences in OA across all biological replicates within our small OA cohort compared to site matched non-OA control tissues, while several additional candidates trended toward significance. In an effort to expand the potential candidate pool, and to explore the effect of sample heterogeneity and diverse etiology of OA, we furthered our investigation by comparing the medial OA patient tissues to their donor matched lateral half of the tibial plateau **(Figure 4A)**. One important motivation behind this comparison is the age-related nature of OA that allows for amounts of age-related damage to accumulate even in histologically “healthy” or non-OA diagnosed patients, as seen by the loss in cartilage thickness of the medial edge of control patient C4 **(Supplemental Figure 5A)**, which may increase variability among the non-OA specimens in this sample pool. This variability may be alleviated by comparing tissue specimens from the same person by utilizing the histologically normal Lateral OA tissue as a separate additional control group. One candidate peptide from ROC analysis, COL1A1 - $G^{305}LP^{ox}GERGRP^{ox}GAP^{(ox)316}$ with m/z at 1211.61, as visualized and quantified across both the lateral and medial halves of C1 and P1 individuals, illustrates this variability **(Supplemental Figure 6A).** This allowed us to visualize the disease continuum for this specific peptide from the least affected CAD Lateral tissues to the proposed equally effected CAD Medial and OA Lateral tissues, on to the most effected OA Medial tissues. While this feature was most highly elevated in OA medial tissue as expected, the next highest intensity was from the cadaveric medial control which had feature intensity significantly higher than even the lateral OA tissue **(Supplemental Figure 6B)**. This suggests there may be difference in disease presentation between the cadaveric medial and OA lateral samples. To further elucidate this, clustering of all Cadaveric Medial tissues to all OA Lateral tissues utilizing the feature intensity of candidates identified by the ROC analysis (**Supplemental Figure 6C**) by PLS-DA showed distinct separation between these two groups. This implies that both the Cadaveric Medial and OA Lateral groups describe distinct populations. Given the difference between the two “control” sets of tissues, the Cadaveric Medial and the OA Lateral that highlight early changes occurring in histologically normal tissues, and the ability to remove patient to patient variability by utilizing tissue-matched samples from the same patient and identify later changes occurring with OA progression, both halves of the tibial plateau from representative OA patient P1 were loaded into the same SCiLS data processing workspace to begin this new analysis. A composite spectrum was generated from data acquired from the two separately imaged tissue slides that represents the combined 64,183 individual

spectra across the entire tibial plateau of OA patient P1. Region segmentation **(Figure 4B)** was again performed that recapitulated similar bone regions in the Medial OA section as before, including the diseased bone region on the most medial edge (red) and a progressive change towards a bone type with a heathier appearance further down into the subchondral trabecular bone in the lateral joint (yellow, orange). Interestingly, this diseased bone signature extends well into the lateral side of the joint where a thick cartilage layer remains and is not limited to only the area of cartilage loss on the medial edge. The segmented regions containing the diseased bone and the healthier bone were isolated and a discriminating feature analysis utilizing the ROC curve prediction method was performed to generate candidate features with an AUC > 0.85. A heat map for the example candidate peptide COL1A1 - $G^{626}PAGERGEQ^{634}$ with m/z at 900.40, found in the previous site-matched comparison, also found in this comparison with an AUC of 0.872, is shown **(Figure 4C)** beside its ROC curve to illustrate how well the distribution of the candidate features from this analysis align to the boundaries of the segmented regions. This analysis generated 34 candidate features **(Supplemental Table 3)** with an AUC > 0.85 each with their own spatial distributions **(Figure 4D)**. Of these 34 candidate features, 19 of these features were previously identified in the earlier site-matched comparison including several peptides of COL1A1 but also peptides belonging to keratins, fibronectin, and COL6A1 and COL6A3, all important structural proteins that enforce ECM stiffness. Keratin 2 (KRT2), the protein of the specific peptide detected, has previously been reported as one of six specific proteins upregulated in extracellular vesicles in synovial fluid of osteoarthritic patients, while Collagen type VI is implicated in the mechanotransduction response of articular cartilage and may regulate chondrocyte pericellular matrix properties that can change in disease [53, 54]. This comparison resulted in an additional 15 candidates identified, including additional peptides of COL3A1 and COL6A3 as well as the member of the cartilage matrix ASPN, by using the tissue-matched controls, resulting in a total of 44 candidates from both comparisons **(Supplemental Table 3)**. To verify that the candidate lists were not overly sample-specific, this same candidate feature identification process was completed on an additional OA patient **(Supplemental Figure 8)** and this resulted in a similar number of candidate features with the majority of features in both lists. Since the segment tissue region that contains the diseased tissue extends across the joint from the medial into the lateral edge, we sought again to restrict our comparisons to just the outermost regions of the joint to best understand the joint-site specific differences between diseased OA bone and a healthier bone region from the same tissue. New regions of interest (ROIs) were generated containing only the outer portions of bone from the lateral and medial side of the joint using both histology and the automatically generated region segments as guides. Despite these new regions now containing possible mixes of tissue types (marrow, trabecular bone) the predictive AUC from ROC analysis for many of the candidate features, including the depicted bone marker COL1A1 peptide, increased with

the guided segmentation **(Figure 4E).** Statistical comparisons using the four OA patients' medial and lateral tissue joint halves completed the site-matched candidate features. ROIs for each tissue segment were drawn following the same guidelines as before, outlining the subchondral bone from the medial edge to the start of receding cartilage for medial sections and an equivalent amount of bone underneath cartilage in the lateral sections **(Figure 5A).** Raw spectral data from each ROI was exported for each of the 44 candidate features and the average pixel intensity based on peak height for each ROI was calculated. A PLS-DA based on all 44 candidate features and their average peak intensity per tissue section **(Figure 5B)** showed that OA lateral group samples cluster away from the OA medial samples despite them originating from the same tissues, highlighting the severity of disease and tissue remodeling occurring in the medial OA tissue. Utilizing all 44 features for these comparisons gave us a more comprehensive look at the molecular regulation occurring in OA, for instance, the candidate COL1A1 peptide $G^{305}LP^{(ox)}GERGRP^{(ox)}GAP^{(ox)316}$ with m/z at 1211.60, initially only identified by comparing OA Medial P1 to Cadaveric Medial C1 did not show significance at our small N=4 for the OA Medial to Cadaveric Medial comparisons ($p = 0.229$), but was significantly elevated in the OA cohort when comparing OA Medial to OA Lateral ($p = 0.031$), showing the utility of limited patient-patient variability in studies using smaller patient cohorts **(Supplemental Table 3).** In statistical comparisons of the OA Medial tissues vs their Lateral tissue-matched controls using a paired t-test, 31 of the 44 candidate features showed significant differences, with an additional 7 features trending towards significance **(Supplemental Figure 8)**. Of the 44 candidates, 36 feature m/z's matched to peptide identifications within 2 mDa of their theoretical mass from studies of breast, lung, and heart tissues with this same enzyme digestion [20, 41, 46] **(Supplemental Table 3)**. Of the eight unmatched candidates, five reached significance levels in the group-wise comparison suggesting these may be novel bone-specific markers of OA and joint disease that will require further classification and identification. Of the statistically elevated candidates in OA Medial vs Lateral tissues with known peptide identifications, four peptides belonging to proteins that have been seen in proteomics of synovial fluid from OA patients (data not shown) are depicted **(Figure 5C)**. These include peptides for fibrillar collagens COL3A1 and COL1A1, the network forming COL6A1, and a member of the cartilage ECM, Asporin. Each of these peptides increase in their abundance within the diseased medial subchondral bone when compared to their lateral tissue-matched controls. Revisiting the earlier OA medial to Cadaveric medial comparison with the full list of 44 candidates, 5 additional markers not previously seen by screening OA medial to Cadaveric medial alone now trend toward elevation ($0.05 > p > 0.1$) and 1 additional feature is significantly elevated in this cohort **(Supplemental Figure 9)**. While a marginal improvement, this demonstrates the importance of utilizing multiple controls to accurately study such a diverse disease as OA. Using the full set of 44 candidate features from both site-matched and tissue-matched comparisons across the patient

cohort, we see a similar and robust upregulation of potential damage maker proteins in OA tibial plateaus whether compared to site-matched or tissue-matched control tissues. Overall, we demonstrate the capabilities for MALDI-MSI and an ECM specific collagenase-based enzymatic digestion to detect novel markers of osteoarthritis progression in the subchondral bone of human knee tibial plateaus.

Mapping Post-translational Modifications – Enrichment of Collagen Crosslinking in OA

One important mechanism in bone development and remodeling is the tightly regulated series of post-translational modifications that is required for the self-assembly of collagen fibrils. This self-assembly requires the oxidation of specific proline residues along the peptides of different collagen subtypes and is enzymatically catalyzed by several enzymes, including the family of prolyl hydroxylases [55, 56]. These homeostatic mechanisms are tightly regulated in healthy bone and joint tissues but have been implicated as dysregulated in different models of skeletal disease and aging in mice, including in diabetes and in disrupted osteocytic perilacunar/canalicular remodeling [14, 15]. Thus, the ability to detect specific post-translational modifications on distinct amino acids within a protein sequence from skeletal tissue, and the determination of their quantitative differences during disease or aging will be a helpful tool to assess the molecular alterations occurring in aging and disease. MALDI-MSI along with peptide spectral libraries from collagenase III digested tissues demonstrates the ability to detect and visualize matching peptides containing one or more oxidized proline residues in bone tissue. One peptide feature at m/z 1082.63 within the MALDI-MS spectrum was matched to a peptide of COL1A1 with a hydroxyproline (HYP) modification, $I^{954}AGQRGVVGLP^{(ox)964}$, with a small mass error <15 ppm **(Figure 6A)**. Liquid chromatography tandem mass spectrometry (LC-MS/MS) data-dependent acquisitions (DDA) on the timsTOF-HT (Bruker) of collagenase digested tissues recovered from slides after imaging confirmed the identification and site-location of the modified proline, P^{964} in the peptide $IAGQRGVVGLP^{(ox)}$ of Col1A1 on the MS/MS level **(Supplemental Figure 10A),** while spectra for the unmodified peptide were not found in analysis of digested tissue. For peptides where DDA analysis was unable to specifically determine HYP modification location due to multiple potential prolines within a peptide, **Supplemental Table 3** lists the PTM site probabilities as determined by MaxQuant for each modified peptide as reported by other databases [57]. This feature, matching to a modified COL1A1 peptide, displayed high signal intensity in the subchondral region below areas of cartilage loss in an OA patient. Visualization of the MALDI-MS spectrum at the m/z corresponding to this peptide with a replacement of the HYP modification with an unmodified proline at m/z 1066.64 resulted in an image with high signal to noise ratio. A precursor for the unmodified peptide, $I^{954}AGQRGVVGLP^{964}$, was not detected in our LC-MS/MS spectral library. The presence of the modified peptide and non-

detectability of the unmodified form localizing to specific pathologies highlights the importance of proline modifications in defining skeletal collagens.

This integrated workflow of combining MALDI-MS Imaging and ESI-MS/MS spectral library building was used to determine which modified forms of peptides - specifically hydroxy proline-containing peptides - are more abundant with disease or OA. For example, a key feature with m/z at 1426.68 displays a strong spatial profile with localized areas of high intensity near the center of bone trabecula. This feature was identified as a triple-modified peptide of collagen COL1A1, $G^{656}KP^{(ox)}GEQGVP^{(ox)}GDLGAP^{(ox)670}$ **(Figure 6B)**. At the m/z value in the MALDI MS spectrum that corresponds to the same peptide sequence with one less HYP, at m/z 1410.68 corresponding to peptide $G^{656}KP^{(ox)}GEQGVPGDLGAP^{(ox)670}$, a distinct peak is also observed that results in a spatially resolved image resembling the triple-modified peptide including similar regions of signal intensity within the central areas of trabecular bone. LC-MS/MS DDA analysis confirmed the presence of precursor ions in our data set with three modified prolines **(Supplemental Figure 10B)** and two modified prolines **(Supplemental Figure 10C)** for this COL1A1 peptide sequence. The MS/MS spectra for the doubly HYP modified peptide was even able to specifically localize the position of the two HYP modifications to prolines P658 and P670. Attempts to assay this peptide with fewer modified HYPs, corresponding to peptides at m/z 1394.68, representing the same base peptide with 1 HYP, and m/z 1378.68, representing the unmodified peptide, resulted in no discernable identifications in the MALDI MS spectrum above background. Additionally, precursor ions for these latter species (unmodified or only 1 modifications) were not found in the assembled LC-MS/MS spectral library suggesting high levels of hydroxyprolines and reduced or undetectable amounts of unmodified peptides for COL1A1, one of the major components of the bone ECM matrix. Comparisons utilizing the OA cohort **(Supplemental Figure 11A)** for these peptides and all its modified forms starting with the triple modified form, $G^{656}KP^{(ox)}GEQGVP^{(ox)}GDLGAP^{(ox)670}$ with m/z at 1426.68 **(Supplemental Figure 11B,** 3xHYP**)** and then the next least modified peptide **(Supplemental Figure 11C-E**, 2x, 1x and 0x HYP**)** showed that the more modified forms with three or two HYPs were the most represented in diseased tissue **(Supplemental Figure 11F)**. While MALDI-MSI may be able to detect signal for m/z potentially corresponding to the lower HYP modified peptides with m/z at 1394.68 and 1378.68, it is important to note that their average pixel intensities are very low not reaching above the surrounding signal to noise S/N background, and almost 30 times lower than the triple-modified peptide. This suggests that overall, peptides containing multiple HYP modifications are more predominant in bone material that clearly and significantly become over-represented in OA.

Beyond the HYP modifications, peptides found abundant in OA can be involved in other potential crosslinking or PTM mechanisms. For example, the base peptide,

$G^{656}KPGEQGVPGDLGAP^{670}$, from above, contains a documented glycation site at K^{657} [58, 59]. In fact, 22 of the 27 significantly elevated candidate features identifying as belonging to Col1A1 or Col1A2 contained glycation or other known locations of collagen post-translational modifications that are not ascribed to HYPs when compared to the functional collagen interactome **(Supplemental Table 3)**. Thus, the elevation of PTMs in OA bone compared to controls, and the decrease of the unmodified forms in diseased tissue compared to non-arthritic controls emphasize the loss of subchondral bone homeostasis that occurs in OA. Interestingly, in our analysis of the subchondral bone in OA, no candidate features were significantly down regulated in OA subchondral bone among our clinical cohort. Here we show the effect on subchondral bone in OA is to upregulate certain disease marker peptides. The formation of PTMs along collagen are important steps in the generation and maturation of the bone matrix material and the ability to visually confirm these modified peptides and modification sites expands the utility of MALDI-MSI in investigating skeletal biology.

Discussion

Osteoarthritis is most commonly identified by self-reported pain in patients and by the appearance of osteophytes, or mineralized growths, and by join-space narrowing as revealed by X-rays or Magnetic Resonance Imaging (MRI) scans of affected joints. Even then, full confirmation or grading of the disease state cannot be made until histopathologic stains that can confirm the loss of cartilage and other markers of disease are visualized on post-surgically removed joint tissue, meaning current gold-standard diagnostics are typically only available after intervention. Further, there are currently only limited pre-clinical molecular diagnostics for OA or OA progression that stratify patients who may benefit from early intervention to improve joint health. In this study we demonstrate that matrix assisted laser/desorption ionization (MALDI) mass spectrometry imaging (MSI) may be used as an effective tool for the study of the molecular and biochemical spatial changes that occur in human joint tissues during osteoarthritis (OA) and that knowledge gained from these studies may be aimed at developing molecular diagnostics for disease progression.

We report the first successful protein-based molecular spatial mapping of skeletal tissues composed of both cartilage and bone regions by targeting ECM proteins with an enzymatic strategy utilizing collagenase-III. The feature-rich composite spectrum of collagenase III digested skeletal tissue captured by MALDI-MSI molecularly discriminates bone from cartilage, demonstrating the effectiveness and promise of this technique for studying musculoskeletal disease and its effects on the complexity of the extracellular matrix (ECM). Proteins detected comprise standard ‘marker’ proteins for bone and cartilage, including COL1A1 and COL2A1 respectively, spatially localized to their corresponding tissue types as confirmed by histology. Molecular image processing allowed for an unbiased processing of over several hundred candidate peptide features at once, enabling a

comprehensive workflow for unbiased detection of novel disease markers. Using FFPE sections from the tibial plateau of human donors who had received knee replacement and site-matched tissues from non-arthritic age and BMI matched cadaveric donors, we find specific peptides belonging to ECM proteins that are upregulated in OA, including peptides belonging to less common collagens such as COL3A1 and COL6A3. Though commonly seen in muscle and tendon, in the pericellular matrix around chondrocytes [60], and in young actively remodeling bone [61], this is, to our knowledge, the first documented detection of collagen type (VI) in aged-human arthritic bone. This adds to a growing base of knowledge of the role of collagen type (VI) as a fibrotic biomarker outside its role in tissue development [62], now specifically in OA. This panel of peptide markers was expanded by utilizing the less affected lateral half of joints from the same OA donors as patient and tissue matched controls. This limited person-to-person variability and allowed for the validation of over 30 specific peptides that were significantly upregulated in medial OA tissues compared to either Cadaveric medial or OA lateral controls. The identification of protein level regulation in the subchondral bone of OA suggests that molecular remodeling on the protein level occurs throughout the process of joint degeneration in addition to alterations to bone density and bone mass. Knowledge of how different peptide regions of ECM proteins are altered in disease provides needed biologic context for the mechanical and biochemical changes occurring in OA diseased tissues that may directly influence resident cell types, as well as the potential ability to use these potential peptides as therapeutic or diagnostic biomarkers in future studies. This study provides both the first successful application of MALDI-MSI, and a validated protocol, for protein-based imaging on composite joint tissues including both cartilage and bone, as well biologic insight into joint disease on the protein and molecular level which can inform future studies aimed at improving treatment and diagnostics for arthritis.

Technical Achievements and Considerations

Given the mixed tissue types within the joint, such as mineralized bone and the highly hydrated cartilage, no commonly used tissue preparation strategy for MALDI-MSI is appropriate for studying all the different compartments of the joint and different analytes, from small molecule metabolites and lipids to larger proteoglycans, proteins, and peptides. While others have utilized MALDI-MSI to visualize changes to lipids and proteoglycans in bone [29, 33, 35-38, 63] protein-based imaging of joint tissues has been thus far limited to the synovium and cartilage, which even then has resulted in a small number of detected proteins. Partially, this is due to the nature of the skeletal ECM, especially in bone, which is highly crosslinked and post-translationally modified with glycans that altogether act as a physical barrier impeding the access of traditional enzymes used in MS strategies such as trypsin. Thus, our first challenge was to adapt protocols from other tissue contexts that have

successfully targeted the ECM and apply these robust, yet technically challenging processes, to joint tissues composed of bone and cartilage.

The main hurdle of adapting protocols to joint tissue composed of both cartilage and subchondral bone is the difference in material composition of the different subregional tissues and their reaction to traditional sample processing methods. For instance, relative to bone that is at most 25% water, cartilage is essentially a hydrogel composed of nearly 80% water in physiologic conditions. These differences cause the two tissues to react differently to tissue processing. For previous applications of on-slide enzymatic digestions of FFPE tissue slides for MALDI-MSI, a rapid heat induced epitope retrieval (HIER) in aqueous media at high temperatures (95-97 °C) has been used to expose epitopes for enzymatic degradation [43, 45]. For dehydrated bone tissues, the heating of these tissue to nearly boiling in aqueous medias often causes the dissociation of tissue from slide, or a general degeneration of the delicate trabecular bone structure, while hydration of cartilage may cause it to become buoyant and lift from the slide. Thus, care was taken to reduce the temperature of the HIER while we also extended the incubation time to protect bone tissues. While a longer incubation at lower temperature did prove successful, one could not process tissues too long. Any HIER longer than 12 hours destabilized the bone tissue resulting in loss of trabecula. We found that a HIER at 60 °C from 6-8 hours was sufficient to allow for desirable tissue rehydration, epitope exposure, and subsequent enzymatic activity; but exceeding 12 hours at 60 °C resulted in tissue degradation similar to one hour at 95-97 °C. This carefully monitored HIER allowed for tissue sections to remain intact, even after sequential enzymatic digestion steps, including separate HIER for both an initial digestion with Peptide N-Glycosidase F (PNGaseF) to prepare and image glycans species **(Supplemental Figure 3)**, and a second enzymatic preparation with collagenase III that targeted the ECM. Even after protein-based imaging, tissues remained intact and adhered to slides and would have been usable for further sequential digestions using other enzymes, possibly trypsin, among other options [43].

Despite extreme care with the HIER, tissues continued to present technical challenges. For instance, cartilage layers tended to lift from slides, and so flat slide orientations and careful manual washing and cooling by slowly replacing solutions via pipette, instead of rapid solution replacement, was required to maintain cartilage integrity and placement. Even with great care, evidence of tissue folding can be seen in the dislocation of the medial edge of the cadaveric C2 tissue **(Supplemental Figure 1)**. While marginally interfering with the accessibility of the folded edge of this specific sample, this artifact did not impede the collection of MS data from this sample. One potential workaround for these technical complications, commonly used in skeletal tissue histology, is the use of adhesive slides and tapes to counteract tissue folding [64]. While tapes were not used in the present study,

tape systems exist compatible with MALDI MSI that could be deployed in the future for use in bone studies [65, 66]. While further optimization and automation may increase sample throughput by standardizing these rigorous protocols, we have successfully demonstrated that even the extensive and repetitive sample preparation required for proteolytic based MALDI-MSI was successfully applied to skeletal tissues in this study investigating human knee joint tissues, even those affected by OA.

Biologic Ramifications and Significance

Of the many exciting findings from the molecular imaging of subchondral bone in osteoarthritis, one major outcome was the identification of a 'diseased' subchondral bone signature. Here, the enzymatic approach was collagenase based, and it is not surprising that many members of the 46 candidate features of this disease signature identified through ROC discriminating feature analysis had protein identifications that were a form of collagen. However, collagen itself is not merely simply a structural protein. It is well known that the collagen fibril is bioactive and can bind many other proteins or provide Arginine-Glycine-Aspartic (RGD), domains for cellular attachments [58, 59, 67]. By identifying the specific peptides of collagens via highly sensitive mass spectrometry and understanding their spatial localizations with MALDI imaging, we gained novel insights into the changes to biologic activity occurring specifically in the areas of tissue damage in OA. For example, the unmodified COL1A1 peptide $G^{1165}PRGRTGD^{1173}$ with m/z at 1139.58 is significantly increased in the diseased medial regions of our OA patients **(Figure 5C)**. This specific peptide exists towards the C-terminal domain of the collagen 1 triple helix and lies within an area of interleukin 2 (IL2) and amyloid precursor protein (APP) binding [58, 59] **(Supplemental Figure 12A)**. IL2 is a well-known inflammatory marker and enhancer of the T-cell immune response, while APP interaction with collagen 1 has also been shown to enhance cell-matrix adhesion and enhance the function and activation of peripheral monocytes [68, 69]. This peptide also overlaps an area of Phosphophoryn, also known as Dentin phosphoprotein - a protein known to enhance mineralization in the formation of dentin tissue [70]. The implication of proteins involved in mineral regulation in OA affected tissue provides biologic mechanistic insight of how mineral regulation and subchondral bone thickness alterations may be accomplished in OA, though these interactions remain to be investigated. These novel observations in the context of OA and knowledge of their spatial distribution specifically in the subchondral bone beneath areas of cartilage loss provide new insights into the cellular and molecular interactions that may be occurring in disease and promote further investigation of the biologically regulatory features of 'structural' collagen in the context of this disease.

Other collagen I peptides were identified as upregulated in OA when compared against non-arthritic, cadaveric controls or histologically normal lateral joint tissues, and those were identified with post-translational modifications. In addition to the COL1A1 peptide

$G^{656}KP^{(ox)}GEQGVP^{(ox)}GDLGAP^{(ox)670}$ **(Figure 6B, Supplemental Figure 11)**, the COL1A1 peptide $G^{305}LP^{(ox)}GERGRP^{(ox)}GAP^{(ox)316}$ with m/z at 1211.60 is upregulated in the comparison of medial OA to lateral OA **(Supplemental Table 3)** and contains three hydroxylated proline residues. Hydroxyproline modifications in bone are important for increasing collagen structural integrity and reinforcing the triple helix of the collagen fibril [56, 71], and the upregulation of these modifications in OA may hint at molecular mechanisms impacting the material stiffness of bone in OA joints independently of hypermineralization. Further examples of PTM regulation in OA can be found in other upregulated regions of the collagen type 1 fibril. For example, the peptide of COL1A1 $G^{626}PAGERGEQ^{634}$ at 900.40 m/z within the mature collagen type I fibril is bound to COL1A2 where lysine K343 is a known glycation site **(Supplemental Figure 12B)** [58]. This region of the mature collagen fibril is also thought to bind different keratin sulfate proteoglycans **(Supplemental Figure 12B)**, both important PTMs for collagen [58, 59]. Glycation, in the form of advanced glycation end-products (AGEs), can further stiffen the bone matrix [72] and alterations to proteoglycans in bone, such as in diseases like osteogenesis imperfecta, negatively impact bone strength [73]. Thus, the presence of these modification sites in OA bone where cartilage has worn away implicates post-translational regulation as one mechanism that may alter subchondral bone homeostasis in OA. Interestingly, we find that these PTM changes occur in areas of cartilage loss where it is thought that physical loading of the joint alters throughout the course of disease [74]. It remains to be elucidated whether these changes reflect the mechanical reinforcement of collagen by PTMs in bone underlying areas of cartilage damage or are a mark of underlying disease in bone that gives rise to local cartilage degeneration.

Aside from collagen 1, the presence of other less common collagens comprises a disease signature of OA related peptides in bone. Several peptides of COL3A1, a less common fibrillar collagen active in wound repair, is also upregulated in the diseased subchondral bone of OA patients **(Figure 5C)**. Collagen Type III has also been implicated in the cartilaginous regions of osteoarthritic joints as an attempt by chondrocytes to remodel or stabilize remaining cartilage [75], while in bone it is thought to promote osteoblast differentiation leading to increases in trabecular bone mass [76]. Thus, the upregulation of collagen type III in the subchondral bone of OA tissue compared to control tissue points to a potential role in driving late stage increases to bone mass and trabecular bone sclerosis common in OA [77]. The detection of peptides belonging to Collagen Type VI, including various peptides of COL6A1 and COL6A3 **(Figure 5C, Supplemental Table 3),** may be the first detection of this network forming collagen in adult bone tissue outside the growth plate specifically where chondrocytes aid in bone formation through endochondral ossification [78, 79]. Knockout of the *Col6a2* gene prevented normal ossification of the temporal mandibular joint in mice, suggesting that Collagen Type VI may play important roles in chondrocyte differentiation and bone growth in development [78], however its role in bone in OA is unknown. Collagen type VI, is produced by

hypertrophic chondrocytes in OA cartilage where it modulates pericellular mechanics [53, 60, 80]. Strikingly, our detection of Collagen Type VI in OA subchondral bone, with several peptides from multiple sub-chains - alpha 1 and alpha 3 - hints at an important role for this collagen subtype in OA related bone remodeling and fibrosis. Although precise mechanisms behind this and the cell type responsible for its presence in osteoarthritic bone are currently unknown, the role of Collagen Type VI during bone development implies that this collagen subtype may mark the effort to mount a regenerative response, which ultimately leads to subchondral bone sclerosis in OA. While the 44 peptide disease signature contains many different collagen peptides, the specific peptide identity and their functional and biological roles offer insight in the cellular and molecular mechanisms at play in subchondral bone in OA.

Another significant insight offered by this OA imaging study is direct visualization of the spatial distribution of the 'diseased' subchondral bone. While it is intuitive that damage and associated changes to the ECM would be most highly constrained to areas of subchondral bone underneath lost cartilage, proteome-wide profiling of altered bone ECM composition has not before been achieved. Utilizing a collagenase III (MMP13) enzymatic based approach, an unbiased analysis of subchondral bone protein changes in OA can be visualized for the first time. These changes primarily occur in areas where osteocyte dysfunction and subchondral bone sclerosis have been described histologically and radiographically **(Supplemental Figure 1),** as demonstrated in previous studies on this cohort of patients [7]. While this disease signature is most evident in areas underlying cartilage loss, imaging of the lateral half of OA joints reveals that the disease signature emerges even in subchondral bone areas where a thick cartilage layer remains **(Figure 4B-C red, Figure 5C)**. Given that osteocyte dysfunction can play a causal role in OA, it will be important to further investigate the cellular origins of this altered proteomic signature[7, 81]. Such studies may elucidate the extent to which progression of OA arises from altered joint mechanical loading, changes in cellular metabolic or secretory behavior, or altered signaling by resident skeletal or immune cell populations. The possibility that lost subchondral bone homeostasis can precede cartilage damage should focus the search for early OA diagnostics on bone. Thus, the continued investigation into subchondral bone changes, especially at earlier ages, among a larger cohort of individuals is warranted. Additionally, the current OA cohort only included tissues from male patients in the Veteran's Administration healthcare system. Given that OA has an increased prevalence in females[1, 2], proteomic profiling of OA in female joints is essential. Despite these concerns, this study defines a new protocol that enables application of MALDI-MSI to bone and defines proteomic changes that provide novel insight into the molecular progression of OA in subchondral bone.

Conclusions and Future Outlook

Further studies that implement MALDI-MSI to investigate the progression of human OA may be completed to extend the impact of this technological advance. First, the identification of novel candidate peptides that are upregulated in our OA cohort that currently do not have matching IDs in other tissue ECM specific digestions warrant more extensive efforts to build joint-specific peptide libraries for the identification of novel biomarkers of disease. By continuing to build libraries from collagenase digested skeletal tissue we can more accurately identify these outstanding OA marker proteins to build more comprehensive peptide libraries of disease markers. Additionally, the promising success of this collagenase-based imaging motivates the use for other serial enzymatic digestions including elastases and chondroitinases [43] that can further probe the compositional changes of the ECM in OA. Excitingly, our new molecular evidence supports previous morphologic findings from uCT and MRI that subchondral bone in OA undergoes dramatic molecular remodeling, and these changes to subchondral bone can occur in bone even before cartilage loss in some cases [5, 6, 10]. Thus, we suggest continued effort be spent in understanding the changes to subchondral bone as a way to develop diagnostics and treatments for Osteoarthritis.

Utilizing larger cohorts of individuals with OA, at multiple disease stages or ages, comprehensive knowledge of the molecular landscape of OA may be assembled and potential disease or skeletal damage biomarkers uncovered **(Supplemental Figure 13)**. Our study is limited in that this OA cohort is comprised of a small number of end-stage disease OA patients receiving joint replacement. The extension of this technique to mouse models of OA where the biologic replicates can be easily increased, and disease progression and OA stage may be controlled or more longitudinally monitored would provide much needed time courses and new hallmarks of early disease and tissue remodeling. Classification of the protein changes occurring in subchondral bone early in disease, prior to cartilage loss or the clinical presentation of pain, would greatly enhance the ability to develop diagnostics. Given that OA is also a naturally age-related disease, monitoring tissues of healthy donors across multiple ages may also provide some data on the early progression of OA. Even within the non-arthritic cadaveric donors, many of the original “candidate” features showed high signal in individual control tissues. This highlights the heterogeneity of OA and how potential disease markers may be detected in non-arthritic aged individuals even without a clinical OA diagnosis. Thus, future studies in a larger cohort of “healthy” aged donors are warranted.

Targeted studies to understand the mechanism of tissue breakdown in OA and how these markers arise in the natural process of disease is also warranted and will help to solidify our knowledge of OA. Given the proteolytic environment of OA, naturally cleaved peptides are likely to exist in the synovial fluid of inflamed OA joints, and these peptides may even make it to circulation. Thus, by tracking markers that increase with OA in subchondral bone, we can see a path towards the development of highly sensitive and specific diagnostics for a disease that currently severely lacks

reliable early detection methods. In addition, using knowledge gained from foundational studies, such as this, larger panels of candidate peptides can be screened in larger, healthy human populations from biofluids such as synovial fluid and plasma **(Supplemental Figure 13)**. This circumvents the inherent difficulty of analyzing joint tissues from healthy people. Overall, this study provides foundational knowledge about the progression of joint disease, that markers of disease are detectable in the subchondral bone and may be evident prior to cartilage loss, and that novel, specific regions of common ECM proteins may be hallmarks of this damage. Thus, by defining the spatial molecular landscape of OA on the protein level, this study advances new opportunities to increase the specificity of disease diagnostics and biomarkers for OA and opens new opportunities for future works with potential to establish new modes of disease tracking in human osteoarthritis.

Materials and Methods

Human donor population and knee joint specimen preparation

Human knee joint tissues were obtained as described from the University of California, San Francisco, UCSF, as pre-prepared formalin fixed paraffin embedded (FFPE) tissue sections from an existing tissue bank [7]. Briefly, knee joint tissues were acquired as follows: four male subjects with clinically diagnosed stage IV Osteoarthritis of the medial tibial plateau of the knee, who were scheduled for total knee arthroplasty, with an age range from 64 – 79 years old were recruited for this study **(see Supplemental Table 1, Figure 1A)**. Recruitment occurred through referral from orthopedic surgeons at the Department of Veterans Affairs Medical Center (San Francisco, CA, USA). All samples were collected with informed consent from patients with OA of the femorotibial joint as described in protocols that were reviewed and approved by the Human Subjects Protection Program Institutional Review Board of UCSF and the Department of Veterans Affairs Medical Center [7]. Four freshly harvested cadaveric human tibial plateaus from age-matched male donors without history of OA, osteonecrosis, osteoporosis, or fractures were collected through the Willed Body Program at the University of California, San Francisco for use as controls **(see Supplemental Table 1)**. Patients with OA and non-arthritic cadaveric controls had a similar range of body mass index (BMI) and age. Specimens were stratified by their Osteoarthritis Research Society International (OARSI) grade by pathology experts **(Supplemental Figure 1,2).** All samples were harvested within 4 days postmortem to minimize effects of degradation. Specimens were sagittally divided into their medial and lateral halves through the posterolateral root of the posterior cruciate ligament. Tibial plateau tissue slabs composed of both the cartilage and the subchondral bone regions were compared between i) the medial and lateral regions of interest from the same individual, as well as ii) site-matched regions of OA and cadaveric, control tibial plateaus **(Figure 1B)**. Groupwise data were

collected from four biological replicates per each of the 4 study groups for all outcomes (OA medial, OA lateral, cadaveric medial, cadaveric lateral).

Tissue Preparation and Sectioning

Human tibial plateaus were fixed in 10% neutral buffered formalin (NBF) and incubated in an Ion Exchange Decalcification Unit (American Master Technologies) for 5–6 days until fully demineralized. Serial ethanol dehydration and paraffin infiltration and embedding was performed to generate FFPE tissue blocks. Tibial plateaus were sectioned onto standard pathology microscopy slides at 7 µm thickness in the coronal plane. Histological Safranin-O / Fast Green stain **(Supplemental Figure 1)** was used to identify regions of cartilage and cartilage damage in tissue sections. Unstained neighboring tissue sections were selected for Matrix Assisted Laser Desorption Ionization – Mass Spectrometry Imaging (MALDI-MSI) preparation and imaging.

MALDI-MSI for ECM Imaging

Tissue slide preparation and enzymatic digestion followed previously published protocols [23, 43, 45] **(Figure 1C)** with important modifications in consideration of the human tibial plateaus. The slides were heated at 60 °C for 1 hour to melt off excess paraffin wax. After cooling, tissue sections were further deparaffinized by washing twice in xylene (3 minutes each). Tissue sections were washed and rehydrated by submerging in 100% ethanol twice (1 minute each), once in a Carnoy's solution (60% ethanol, 30% chloroform and 10% glacial acetic acid), to remove excess fat and wax, once in 95% ethanol (one minute), once in 70% ethanol (one minute), and twice in water (3 minutes each). After the rehydration series, slides were transferred to a slide mailer containing citraconic anhydride buffer (Thermo) at pH 3.0 for heat induced antigen/epitope retrieval. The slide mailer was sealed and gently arranged in a 60 °C oven so that submerged slides were positioned face up while the mailers were additionally submerged in a larger container (glass beaker) containing buffer that allowed for their orientation and provided an additional buffer reservoir, and left to incubate overnight, not exceeding 12 hours. This extended antigen retrieval at a lower temperature was optimized to maintain the effectiveness of releasing epitopes without disturbing the fragile skeletal ECM also ensuring that the tissues would not detach from the slide. Slide mailers were then removed from the oven and allowed to cool on the bench top. Citraconic buffer was slowly exchanged with water, as to not impact the tissue, five times by removing half of the buffer via pipette and replacing with water, prior to replacing completely with water for the final solution exchange. Deglycosylation was achieved by applying a 0.1 µg/µL PNGase F solution (N-Zyme Scientifics) via the TM Sprayer M3 (HTX Imaging, Chapel Hill, NC, USA), followed by incubation in custom humid chambers for 2 hours at

37°C. After deglycosylation, slides were coated with a 7 mg/mL solution of alpha-cyano-4-hydroxycinnamic acid (CHCA) 50% acetonitrile, 0.1% trifluoracetic acid matrix solution via the TM Sprayer M3. Slides were then first imaged for spatial glycans (**Supplemental Figure 3, Supplemental Table 2**), and then washed carefully with 70% ethanol to remove applied CHCA matrix, a high pH buffer (10 mM Tris, pH 9, and low pH buffer, 10 mM citraconic anhydride, pH 3, followed by distilled water to remove glycans and residual enzyme. Following the wash, slides were vacuum dried in a desiccator and prepared for ECM peptide imaging performing a second epitope retrieval (10 mM Tris, pH 9 overnight at 60 °C), and subsequent application of a proteolytic enzyme: 0.1 µg/µL collagenase III consisting of COLase3 (*Clostridium histolyticum*) Worthington Biochemical (Lakewood, NJ, USA) [47, 48] solution via the TM Sprayer M3, and incubation for 5 hours in humid chambers at 37 °C. After incubation, slides were vacuum dried in a desiccator and coated with CHCA matrix (7 mg/mL solution of alpha-cyano-4-hydroxycinnamic acid (CHCA) 50% acetonitrile, 1.0% trifluoracetic acid).. The CHCA matrix solution was spiked with [Glu1]-fibrinopeptide B human (GluFib) (Sigma-Aldrich, St Louis, MO, USA) for a total concentration of 200 fmol/L. After matrix drying for 30 minutes in a desiccator, the slides were rapidly immersed in cold 5 mM ammonium phosphate, monobasic for <1 second and immediately dried in a desiccator.

Mass Spectrometry Imaging

Mass spectrometric imaging data after proteolytic digestion with collagenase III was acquired using a Trapped Ion-Mobility Time-of-Flight Mass Spectrometer, the timsTOF fleX (Bruker Scientific, LLC, Bremen, Germany) equipped with a dual ESI/MALDI source. Samples were scanned across a MS1 mass range of 600 – 4000 m/z. The SmartBeam 3D 10 kHz laser was set to 20% power, scan range of 20 µm for X and Y and resulting field size of 24 µm for X and Y. 300 spectra were collected per pixel spot. Additional instrument parameters for the studies included: an ion transfer time of 75.0 µs, pre pulse storage time of 20 µs, a collision RF of 2500 Vpp, a collision energy of 25 eV, an ion energy in the quadrupole of 5.0 eV, a TIMS funnel 1 RF of 400 Vpp, a TIMS funnel 2 RF of 500 Vpp and a multipole RF of 400 Vpp. After MS acquisition, the data was imported into SCiLS Lab MVS v2024a Pro (Bruker Scientific, LLC, Bremen, Germany).

Tissue Preparation and Electrospray Ionization MS/MS by Data Dependent Acquisition

After imaging, MALDI matrix removed by 70% ethanol wash. Tissue was removed from slides and fully digested in solution with the same collagenase III used to prepare slides for imaging. Excess enzyme removal and desalting of digested peptides were completed by sequential stage tip and ZipTip (Merk Millipore, Burlington MA) purification. Samples (100 ng) were loaded onto EvoTips Pure

(Evosep, Odense, Denmark) following manufacturer's protocol. LC-MS/MS analyses were performed on an Evosep One liquid chromatography system (Evosep) coupled to a timsTOF HT mass spectrometer (Bruker, Bremen, Germany). The solvent system consisted of 0.1% formic acid (FA) in water (solvent A) and 0.1% FA in ACN (solvent B). Peptides were eluted on a PepSep C_{18} analytical column (150 µm x 15 cm, 1.5 µm particle size; Bruker) using the 30 SPD method (44-minute gradient length, 500-nL/min flow rate). A zero-dead volume emitter was installed in the nano-electrospray source (CaptiveSpray source, Bruker Daltonics) and the source parameters were set as follows: capillary voltage 1600 V, dry gas 3 L/min, and dry temperature 180°C. Each sample was acquired in data dependent acquisition (DDA) - parallel accumulation–serial fragmentation (PASEF) [82] mode with 4 PASEF MS/MS ramps and with the trapped-ion mobility (TIMS) mobiligram inclusion parallelogram expanded to include monocharged precursor ions (Supplemental Table 4). For DDA-PASEF with TIMS on, MS1 and MS2 spectra were acquired over an m/z range of 100-1700 m/z and an ion mobility range of 0.85 -1.70 Vs/cm^2. Precursor ions were selected fragmentation with charge state from 0 to 5, target intensity of 12,500, and intensity threshold of 500. The dual TIMS analyzer was operated in a 100% duty cycle with equal accumulation time and ramp time of 150 ms each, for a total cycle time of 0.78 s. The collision energy was defined as a linear function of mobility starting from 20 eV at 1/K0 = 0.6 Vs/cm^2 to 59 eV at 1/K0 = 1.6 Vs/cm^2. For calibration of ion mobility dimension, three ions of Agilent ESI-Low Tuning Mix ions were selected (m/z [Th], 1/K0 [Vs/cm^2]: 622.0289, 0.9915; 922.0097, 1.1986; 1221.9906, 1.13934). Spectral libraries from acquisitions were generated utilizing Spectromine version 4.0 (Biognosys AG, Schlieren, Switzerland) using a nonspecific enzymatic digestion with peptide length of 7-52 amino acids, with fixed cysteine carbamidomethyl modifications and variable N-terminal protein acetylation and oxidation of methionine and proline. Protein, peptide, and PSM FDR were set to 0.01. Searches were made against a Human UniProtKB/SwissProt reviewed database downloaded from UniProt on April 3, 2023, containing 1032 entries of proteins with "Extracellular Matrix" GO cellular component annotation. Finally, the best 3-6 fragments per peptide were kept. MS/MS spectra for hydroxyproline containing peptides were manually inspected and verified in Skyline-daily v21.2.1.535 (University of Washington, WA, USA) [83]. The final newly generated spectral library contained 543 peptides, 320 of which contained hydroxyproline modifications, all corresponding to 58 protein groups, all spectra were manually reviewed.

MS Imaging Data Processing and Statistical Analysis

Image processing and mass spectrometry data analysis was completed in SCiLS Lab MVS v2024a Pro (Bruker Scientific, LLC, Bremen, Germany). Each tissue section was independently processed and normalized to the glufibrinogen (GluFib) standard peptide at m/z 1570.6768. We used the top

500 most abundant m/z features from each tissue to automatically detect and generate tissue regions through a Bisecting K-means method using the Segmentation operation within SCiLS Lab [84]. The number of hierarchical regions generated was set to the minimum required to identify cartilage regions from bone and to resolve subchondral trabecular bone against the background or marrow space areas. This unsupervised processing typically generated 4 to 6 tissue subregions often identifying multiple transitional bone subtypes. We used a representative tissue section of the more diseased medial site from a specific OA patient (patient #1, P1), its own matched lateral control tissue, and a representative non-arthritic medial section from a cadaveric control (control #1, C1) to perform paired Discriminating Feature analysis [52, 85, 86] within SCiLS Lab. These analyses processed all 30,000-40,000 captured spectra per imaged tissue (specific number of spectra differed by tissue size per sample) to identify candidate marker features (m/z) defining the difference between identified non-arthritic and diseased subchondral bone regions in both site and tissue-matched comparisons. Candidate markers were considered if the area under the receiver operating curve (ROC) generated by the Discriminating Feature analysis for a given m/z was ≥0.85. Similar sets of candidate peptides were generated using tissue sections from different individuals **(Supplemental Figure 7).** The automated tissue segments from SCiLS Lab along with the 'neighboring' histologic stains of serial tissue sections were used to draw regions of interest (ROIs) manually. These ROIs included the diseased regions of subchondral bone to the edge of exposed cartilage on the medial side in OA patients or an equal distance of subchondral bone of the lateral side of the tissue matched joint **(Figure 5A)**, or ~2/5 the length of subchondral bone in cadaveric controls from the medial edge towards the center (the approximate distance of lost cartilage in medial OA samples) **(Supplemental Figure 5)**. The individual pixel intensities by ROI for each candidate m/z feature were exported from SCiLS and the mean pixel intensity was calculated for each candidate feature per each ROI (patient or control sample). Peptide identifications were assigned to m/z features by searching the measured MS1 singly charged precursor ions (M+H) and their m/z value for each feature against previously generated peptide libraries assembled from other tissue types, including breast, cardiac, and lung tissues [20, 41, 46]. Identifications were considered valid if the mass difference between the MALDI feature m/z and the peptide library were ≤ 2 mDa (~15 PPM). In some cases, multiple database sequences matched candidate feature m/z's, in these cases the multiple ID sequences are reported **(Supplemental Table 3),** but statistical analysis considers these as a single candidate feature for reporting purposes. Further MS/MS is needed to further generate tissue-specific peptide sequence matches. MetaboAnalyst v5.0 [87] was used to generate three dimensional partial least squares-discriminant analysis (PLS-DA) plots using mean feature pixel intensity from the combined set of unique candidate features obtained through ROC analysis for each group comparison type. Although

some candidate features were originally found from ROC analysis in one comparison or another (OA Medial vs CAD Medial or OA Medial vs OA Lateral), they exist as detectable features in all samples and statistical testing for group-wise comparisons between OA medial and the two control groups utilized the full 44 feature list. Group-wise comparisons of the sample mean intensity for individual candidate features was completed with Prism Version 10.1.1 (GraphPad) utilizing a paired or unpaired one-sided student's t-test as appropriate (e.g., within patient tissue or between different individuals) with significance set *a priori* at $p < 0.05$. A one-side t-test was selected given that intensity distributions from each ROI were right-skewed and intensity values cannot be negative values. Biological replicates of N=4 for all groups.

Data Availability

The human spatial proteomic datasets have been uploaded to the Center for Computational Mass Spectrometry MassIVE repository at UCSD and can be accessed using the following link:

https://massive.ucsd.edu/ProteoSAFe/private-dataset.jsp?task=c8ee2b4247994c4396007e1cffd0bcfb

[Note to reviewers]: To access data prior during revision (before public release) please utilize the following information: MassIVE ID number: **MSV000094448***;* Username: **MSV000094448_reviewer***,* Password: winter.

Acknowledgements

We acknowledge the NIH for support from the following granting agencies and mechanisms: NIA T32 AG000266 (Schurman, PI Ellerby), NIH-OD S10 OD028654 – (PI: Schilling), NIA P01 AG066591 – (PI Ellerby, Core Director: Schilling), NIA U01 AG060906 – (Schilling), NIDCR R01 DE019284 – (PI: Alliston), DOD PRORP W81XWH1810155 (Alliston), NIAMS P30 AR066262 (Alliston), DOD PRORP OR130191 (Alliston), R21AR083065 (Alliston), DOD HT94252310875 (Alliston), NCI R21 CA240148 (PI: Angel). Drs. Alfred Kuo and Thomas Vail supported the study with the experimental design, collection, and original analysis of human tissue samples. Drs. Schurman and Schilling like to recognize the amazing support and memory of Dr. Judith Campisi for her lifelong dedication to science and advocation for scientific trainees, especially in the field of aging biology.

Conflict of Interest.

Dr. Nannan Tao is an employee of Bruker Daltonics. No other authors have any conflict of interest.

References:

1. Fuchs J, Kuhnert R, Scheidt-Nave C. 12-month prevalence of osteoarthritis in Germany. J Health Monit. 2017;2(3):51-6. Epub 20171009. doi: 10.17886/RKI-GBE-2017-066. PubMed PMID: 37168952; PMCID: PMC10165920.
2. Resende VAC, Neto AC, Nunes C, Andrade R, Espregueira-Mendes J, Lopes S. Higher age, female gender, osteoarthritis and blood transfusion protect against periprosthetic joint infection in total hip or knee arthroplasties: a systematic review and meta-analysis. Knee Surg Sports Traumatol Arthrosc. 2021;29(1):8-43. Epub 20181109. doi: 10.1007/s00167-018-5231-9. PubMed PMID: 30413860.
3. Schurman CA, Burton JB, Rose J, Ellerby LM, Alliston T, Schilling B. Molecular and Cellular Crosstalk between Bone and Brain: Accessing Bidirectional Neural and Musculoskeletal Signaling during Aging and Disease. J Bone Metab. 2023;30(1):1-29. Epub 20230228. doi: 10.11005/jbm.2023.30.1.1. PubMed PMID: 36950837; PMCID: PMC10036181.
4. Heidari B. Knee osteoarthritis prevalence, risk factors, pathogenesis and features: Part I. Caspian J Intern Med. 2011;2(2):205-12. PubMed PMID: 24024017; PMCID: PMC3766936.
5. Burr DB, Gallant MA. Bone remodelling in osteoarthritis. Nat Rev Rheumatol. 2012;8(11):665-73. Epub 20120807. doi: 10.1038/nrrheum.2012.130. PubMed PMID: 22868925.
6. Goldring SR, Goldring MB. Changes in the osteochondral unit during osteoarthritis: structure, function and cartilage-bone crosstalk. Nat Rev Rheumatol. 2016;12(11):632-44. Epub 20160922. doi: 10.1038/nrrheum.2016.148. PubMed PMID: 27652499.
7. Mazur CM, Woo JJ, Yee CS, Fields AJ, Acevedo C, Bailey KN, Kaya S, Fowler TW, Lotz JC, Dang A, Kuo AC, Vail TP, Alliston T. Osteocyte dysfunction promotes osteoarthritis through MMP13-dependent suppression of subchondral bone homeostasis. Bone Res. 2019;7:34. Epub 20191105. doi: 10.1038/s41413-019-0070-y. PubMed PMID: 31700695; PMCID: PMC6828661.
8. Hu Y, Chen X, Wang S, Jing Y, Su J. Subchondral bone microenvironment in osteoarthritis and pain. Bone Res. 2021;9(1):20. Epub 20210317. doi: 10.1038/s41413-021-00147-z. PubMed PMID: 33731688; PMCID: PMC7969608.
9. Alliston T, Hernandez CJ, Findlay DM, Felson DT, Kennedy OD. Bone marrow lesions in osteoarthritis: What lies beneath. J Orthop Res. 2018;36(7):1818-25. Epub 20180522. doi: 10.1002/jor.23844. PubMed PMID: 29266428; PMCID: PMC8607515.
10. Namiri NK, Lee J, Astuto B, Liu F, Shah R, Majumdar S, Pedoia V. Deep learning for large scale MRI-based morphological phenotyping of osteoarthritis. Sci Rep. 2021;11(1):10915.

Epub 20210525. doi: 10.1038/s41598-021-90292-6. PubMed PMID: 34035386; PMCID: PMC8149826.

11. Hayami T, Pickarski M, Wesolowski GA, McLane J, Bone A, Destefano J, Rodan GA, Duong LT. The role of subchondral bone remodeling in osteoarthritis: reduction of cartilage degeneration and prevention of osteophyte formation by alendronate in the rat anterior cruciate ligament transection model. Arthritis Rheum. 2004;50(4):1193-206. doi: 10.1002/art.20124. PubMed PMID: 15077302.

12. Cabral WA, Chang W, Barnes AM, Weis M, Scott MA, Leikin S, Makareeva E, Kuznetsova NV, Rosenbaum KN, Tifft CJ, Bulas DI, Kozma C, Smith PA, Eyre DR, Marini JC. Prolyl 3-hydroxylase 1 deficiency causes a recessive metabolic bone disorder resembling lethal/severe osteogenesis imperfecta. Nat Genet. 2007;39(3):359-65. Epub 20070204. doi: 10.1038/ng1968. PubMed PMID: 17277775; PMCID: PMC7510175.

13. Saito M, Marumo K. Effects of Collagen Crosslinking on Bone Material Properties in Health and Disease. Calcif Tissue Int. 2015;97(3):242-61. Epub 20150320. doi: 10.1007/s00223-015-9985-5. PubMed PMID: 25791570.

14. Acevedo C, Sylvia M, Schaible E, Graham JL, Stanhope KL, Metz LN, Gludovatz B, Schwartz AV, Ritchie RO, Alliston TN, Havel PJ, Fields AJ. Contributions of Material Properties and Structure to Increased Bone Fragility for a Given Bone Mass in the UCD-T2DM Rat Model of Type 2 Diabetes. J Bone Miner Res. 2018;33(6):1066-75. Epub 20180222. doi: 10.1002/jbmr.3393. PubMed PMID: 29342321; PMCID: PMC6011658.

15. Schurman CA, Kaya S, Dole N, Luna NMM, Castillo N, Potter R, Rose JP, Bons J, King CD, Burton JB, Schilling B, Melov S, Tang S, Schaible E, Alliston T. Aging impairs the osteocytic regulation of collagen integrity and bone quality. Bone Res. 2024;12(1):13. Epub 20240226. doi: 10.1038/s41413-023-00303-7. PubMed PMID: 38409111.

16. Franck J, Arafah K, Elayed M, Bonnel D, Vergara D, Jacquet A, Vinatier D, Wisztorski M, Day R, Fournier I, Salzet M. MALDI imaging mass spectrometry: state of the art technology in clinical proteomics. Mol Cell Proteomics. 2009;8(9):2023-33. Epub 20090518. doi: 10.1074/mcp.R800016-MCP200. PubMed PMID: 19451175; PMCID: PMC2742436.

17. Walch A, Rauser S, Deininger SO, Hofler H. MALDI imaging mass spectrometry for direct tissue analysis: a new frontier for molecular histology. Histochem Cell Biol. 2008;130(3):421-34. Epub 20080711. doi: 10.1007/s00418-008-0469-9. PubMed PMID: 18618129; PMCID: PMC2522327.

18. Michno W, Wehrli PM, Blennow K, Zetterberg H, Hanrieder J. Molecular imaging mass spectrometry for probing protein dynamics in neurodegenerative disease pathology. J Neurochem. 2019;151(4):488-506. Epub 20181106. doi: 10.1111/jnc.14559. PubMed PMID: 30040875.

19. Hanrieder J, Ljungdahl A, Andersson M. MALDI imaging mass spectrometry of neuropeptides in Parkinson's disease. J Vis Exp. 2012(60). Epub 20120214. doi: 10.3791/3445. PubMed PMID: 22370902; PMCID: PMC3529518.

20. Angel PM, Schwamborn K, Comte-Walters S, Clift CL, Ball LE, Mehta AS, Drake RR. Extracellular Matrix Imaging of Breast Tissue Pathologies by MALDI-Imaging Mass Spectrometry. Proteomics Clin Appl. 2019;13(1):e1700152. Epub 20181214. doi: 10.1002/prca.201700152. PubMed PMID: 30251340; PMCID: PMC6730639.

21. Angel PM, Spruill L, Jefferson M, Bethard JR, Ball LE, Hughes-Halbert C, Drake RR. Zonal regulation of collagen-type proteins and posttranslational modifications in prostatic benign and cancer tissues by imaging mass spectrometry. Prostate. 2020;80(13):1071-86. Epub 20200720. doi: 10.1002/pros.24031. PubMed PMID: 32687633; PMCID: PMC7857723.

22. Heijs B, Holst-Bernal S, de Graaff MA, Briaire-de Bruijn IH, Rodriguez-Girondo M, van de Sande MAJ, Wuhrer M, McDonnell LA, Bovee J. Molecular signatures of tumor progression in myxoid liposarcoma identified by N-glycan mass spectrometry imaging. Lab Invest. 2020;100(9):1252-61. Epub 20200427. doi: 10.1038/s41374-020-0435-2. PubMed PMID: 32341520.

23. Angel PM, Mehta A, Norris-Caneda K, Drake RR. MALDI Imaging Mass Spectrometry of N-glycans and Tryptic Peptides from the Same Formalin-Fixed, Paraffin-Embedded Tissue Section. Methods Mol Biol. 2018;1788:225-41. doi: 10.1007/7651_2017_81. PubMed PMID: 29058228; PMCID: PMC5997529.

24. Tuck M, Grelard F, Blanc L, Desbenoit N. MALDI-MSI Towards Multimodal Imaging: Challenges and Perspectives. Front Chem. 2022;10:904688. Epub 20220509. doi: 10.3389/fchem.2022.904688. PubMed PMID: 35615316; PMCID: PMC9124797.

25. Ogrinc N, Kruszewski A, Chaillou P, Saudemont P, Lagadec C, Salzet M, Duriez C, Fournier I. Robot-Assisted SpiderMass for In Vivo Real-Time Topography Mass Spectrometry Imaging. Anal Chem. 2021;93(43):14383-91. Epub 20211020. doi: 10.1021/acs.analchem.1c01692. PubMed PMID: 34670081.

26. Aichler M, Walch A. MALDI Imaging mass spectrometry: current frontiers and perspectives in pathology research and practice. Lab Invest. 2015;95(4):422-31. Epub 20150126. doi: 10.1038/labinvest.2014.156. PubMed PMID: 25621874.

27. Kriegsmann M, Seeley EH, Schwarting A, Kriegsmann J, Otto M, Thabe H, Dierkes B, Biehl C, Sack U, Wellmann A, Kahaly GJ, Schwamborn K, Caprioli RM. MALDI MS imaging as a powerful tool for investigating synovial tissue. Scand J Rheumatol. 2012;41(4):305-9. Epub 20120529. doi: 10.3109/03009742.2011.647925. PubMed PMID: 22639849; PMCID: PMC3514013.

28. Cillero-Pastor B, Eijkel GB, Blanco FJ, Heeren RMA. Protein classification and distribution in osteoarthritic human synovial tissue by matrix-assisted laser desorption ionization mass spectrometry imaging. Analytical and Bioanalytical Chemistry. 2015;407(8):2213-22. doi: 10.1007/s00216-014-8342-2. PubMed PMID: WOS:000351195800020.

29. Lee YR, Briggs MT, Condina MR, Puddy H, Anderson PH, Hoffmann P, Kuliwaba JS. Mass Spectrometry Imaging as a Potential Tool to Investigate Human Osteoarthritis at the Tissue Level. Int J Mol Sci. 2020;21(17). doi: ARTN 6414 10.3390/ijms21176414. PubMed PMID: WOS:000569737700001.

30. Rocha B, Cillero-Pastor B, Ruiz-Romero C, Paine MRL, Canete JD, Heeren RMA, Blanco FJ. Identification of a distinct lipidomic profile in the osteoarthritic synovial membrane by mass spectrometry imaging. Osteoarthritis Cartilage. 2021;29(5):750-61. Epub 20210211. doi: 10.1016/j.joca.2020.12.025. PubMed PMID: 33582239.

31. Eveque-Mourroux MR, Emans PJ, Zautsen RRM, Boonen A, Heeren RMA, Cillero-Pastor B. Spatially resolved endogenous improved metabolite detection in human osteoarthritis cartilage by matrix assisted laser desorption ionization mass spectrometry imaging. Analyst. 2019;144(20):5953-8. Epub 20190816. doi: 10.1039/c9an00944b. PubMed PMID: 31418440.

32. Haartmans MJJ, Claes BSR, Eijkel GB, Emanuel KS, Tuijthof GJM, Heeren RMA, Emans PJ, Cillero-Pastor B. Matrix-assisted laser desorption/ionization mass spectrometry imaging (MALDI-MSI) reveals potential lipid markers between infrapatellar fat pad biopsies of osteoarthritis and cartilage defect patients. Analytical and Bioanalytical Chemistry. 2023;415(24):5997-6007. doi: 10.1007/s00216-023-04871-9. PubMed PMID: WOS:001040568600005.

33. Schaepe K, Bhandari DR, Werner J, Henss A, Pirkl A, Kleine-Boymann M, Rohnke M, Wenisch S, Neumann E, Janek J, Spengler B. Imaging of Lipids in Native Human Bone Sections Using TOF-Secondary Ion Mass Spectrometry, Atmospheric Pressure Scanning Microprobe Matrix-Assisted Laser Desorption/Ionization Orbitrap Mass Spectrometry, and Orbitrap-Secondary Ion

Mass Spectrometry. Anal Chem. 2018;90(15):8856-64. Epub 20180709. doi: 10.1021/acs.analchem.8b00892. PubMed PMID: 29944823.

34. Seeley EH, Wilson KJ, Yankeelov TE, Johnson RW, Gore JC, Caprioli RM, Matrisian LM, Sterling JA. Co-registration of multi-modality imaging allows for comprehensive analysis of tumor-induced bone disease. Bone. 2014;61:208-16. Epub 20140130. doi: 10.1016/j.bone.2014.01.017. PubMed PMID: 24487126; PMCID: PMC4005328.

35. Fujino Y, Minamizaki T, Yoshioka H, Okada M, Yoshiko Y. Imaging and mapping of mouse bone using MALDI-imaging mass spectrometry. Bone Rep. 2016;5:280-5. Epub 20160929. doi: 10.1016/j.bonr.2016.09.004. PubMed PMID: 28580397; PMCID: PMC5440778.

36. Svirkova A, Turyanskaya A, Perneczky L, Streli C, Marchetti-Deschmann M. Multimodal imaging of undecalcified tissue sections by MALDI MS and muXRF. Analyst. 2018;143(11):2587-95. doi: 10.1039/c8an00313k. PubMed PMID: 29737333.

37. Lee YR, Briggs MT, Kuliwaba JS, Jagiello J, Anderson PH, Hoffmann P. High-Resolution N-Glycan MALDI Mass Spectrometry Imaging of Subchondral Bone Tissue Microarrays in Patients with Knee Osteoarthritis. Anal Chem. 2023;95(34):12640-7. Epub 20230815. doi: 10.1021/acs.analchem.3c00348. PubMed PMID: 37583288; PMCID: PMC10470451.

38. Briggs MT, Kuliwaba JS, Muratovic D, Everest-Dass AV, Packer NH, Findlay DM, Hoffmann P. MALDI mass spectrometry imaging of N-glycans on tibial cartilage and subchondral bone proteins in knee osteoarthritis. Proteomics. 2016;16(11-12):1736-41. doi: 10.1002/pmic.201500461. PubMed PMID: WOS:000379049100017.

39. Cillero-Pastor B, Eijkel GB, Kiss A, Blanco FJ, Heeren RM. Matrix-assisted laser desorption ionization-imaging mass spectrometry: a new methodology to study human osteoarthritic cartilage. Arthritis Rheum. 2013;65(3):710-20. doi: 10.1002/art.37799. PubMed PMID: 23280504.

40. Rocha B, Cillero-Pastor B, Blanco FJ, Ruiz-Romero C. MALDI mass spectrometry imaging in rheumatic diseases. Biochim Biophys Acta Proteins Proteom. 2017;1865(7):784-94. Epub 20161011. doi: 10.1016/j.bbapap.2016.10.004. PubMed PMID: 27742553.

41. Angel PM, Bruner E, Bethard J, Clift CL, Ball L, Drake RR, Feghali-Bostwick C. Extracellular matrix alterations in low-grade lung adenocarcinoma compared with normal lung tissue by imaging mass spectrometry. J Mass Spectrom. 2020;55(4):e4450. Epub 20200221. doi: 10.1002/jms.4450. PubMed PMID: 31654589; PMCID: PMC7145762.

42. Clift CL, McLaughlin S, Munoz M, Suuronen EJ, Rotstein BH, Mehta AS, Drake RR, Alarcon EI, Angel PM. Evaluation of Therapeutic Collagen-Based Biomaterials in the Infarcted Mouse

Heart by Extracellular Matrix Targeted MALDI Imaging Mass Spectrometry. J Am Soc Mass Spectrom. 2021;32(12):2746-54. Epub 20211029. doi: 10.1021/jasms.1c00189. PubMed PMID: 34713699; PMCID: PMC8639787.

43. Clift CL, Drake RR, Mehta A, Angel PM. Multiplexed imaging mass spectrometry of the extracellular matrix using serial enzyme digests from formalin-fixed paraffin-embedded tissue sections. Anal Bioanal Chem. 2021;413(10):2709-19. Epub 20201118. doi: 10.1007/s00216-020-03047-z. PubMed PMID: 33206215; PMCID: PMC8012227.

44. Clift CL, Mehta A, Drake RR, Angel PM. Multiplexed Imaging Mass Spectrometry of Histological Staining, N-Glycan and Extracellular Matrix from One Tissue Section: A Tool for Fibrosis Research. Methods Mol Biol. 2021;2350:313-29. doi: 10.1007/978-1-0716-1593-5_20. PubMed PMID: 34331294.

45. Angel PM, Comte-Walters S, Ball LE, Talbot K, Mehta A, Brockbank KGM, Drake RR. Mapping Extracellular Matrix Proteins in Formalin-Fixed, Paraffin-Embedded Tissues by MALDI Imaging Mass Spectrometry. J Proteome Res. 2018;17(1):635-46. Epub 20171211. doi: 10.1021/acs.jproteome.7b00713. PubMed PMID: 29161047; PMCID: PMC6637938.

46. Angel PM, Baldwin HS, Gottlieb Sen D, Su YR, Mayer JE, Bichell D, Drake RR. Advances in MALDI imaging mass spectrometry of proteins in cardiac tissue, including the heart valve. Biochim Biophys Acta Proteins Proteom. 2017;1865(7):927-35. Epub 20170321. doi: 10.1016/j.bbapap.2017.03.009. PubMed PMID: 28341601; PMCID: PMC5527275.

47. Eckhard U, Huesgen PF, Brandstetter H, Overall CM. Proteomic protease specificity profiling of clostridial collagenases reveals their intrinsic nature as dedicated degraders of collagen. J Proteomics. 2014;100(100):102-14. Epub 20131011. doi: 10.1016/j.jprot.2013.10.004. PubMed PMID: 24125730; PMCID: PMC3985423.

48. Eckhard U, Schonauer E, Nuss D, Brandstetter H. Structure of collagenase G reveals a chew-and-digest mechanism of bacterial collagenolysis. Nat Struct Mol Biol. 2011;18(10):1109-14. Epub 20110925. doi: 10.1038/nsmb.2127. PubMed PMID: 21947205; PMCID: PMC3191118.

49. Babatunde OA, Pearce JL, Jefferson MS, Frey LJ, Angel PM, Drake RR, Allen CG, Lilly MB, Savage SJ, Hughes Halbert C. Racial Distribution of Neighborhood-Level Social Deprivation in a Retrospective Cohort of Prostate Cancer Survivors. Diseases. 2022;10(4). Epub 20221003. doi: 10.3390/diseases10040075. PubMed PMID: 36278574; PMCID: PMC9589959.

50. Sandhu A, Rockel JS, Lively S, Kapoor M. Emerging molecular biomarkers in osteoarthritis pathology. Ther Adv Musculoskelet Dis. 2023;15:1759720X231177116. Epub 20230619. doi: 10.1177/1759720X231177116. PubMed PMID: 37359177; PMCID: PMC10288416.

51. Cook NR. Statistical evaluation of prognostic versus diagnostic models: beyond the ROC curve. Clin Chem. 2008;54(1):17-23. Epub 20071116. doi: 10.1373/clinchem.2007.096529. PubMed PMID: 18024533.

52. Hoo ZH, Candlish J, Teare D. What is an ROC curve? Emerg Med J. 2017;34(6):357-9. Epub 20170316. doi: 10.1136/emermed-2017-206735. PubMed PMID: 28302644.

53. Zelenski NA, Leddy HA, Sanchez-Adams J, Zhang J, Bonaldo P, Liedtke W, Guilak F. Type VI Collagen Regulates Pericellular Matrix Properties, Chondrocyte Swelling, and Mechanotransduction in Mouse Articular Cartilage. Arthritis Rheumatol. 2015;67(5):1286-94. doi: 10.1002/art.39034. PubMed PMID: 25604429; PMCID: PMC4414817.

54. Foers AD, Dagley LF, Chatfield S, Webb AI, Cheng L, Hill AF, Wicks IP, Pang KC. Proteomic analysis of extracellular vesicles reveals an immunogenic cargo in rheumatoid arthritis synovial fluid. Clin Transl Immunology. 2020;9(11):e1185. Epub 20201107. doi: 10.1002/cti2.1185. PubMed PMID: 33204424; PMCID: PMC7648259.

55. Kühn K. The Classical Collagens: Types I, II, and III. In: Mayne R, Burgeson RE, editors. Structure and Function of Collagen Types: Academic Press; 1987. p. 1-42.

56. Krane SM. The importance of proline residues in the structure, stability and susceptibility to proteolytic degradation of collagens. Amino Acids. 2008;35(4):703-10. Epub 20080423. doi: 10.1007/s00726-008-0073-2. PubMed PMID: 18431533.

57. Tyanova S, Temu T, Cox J. The MaxQuant computational platform for mass spectrometry-based shotgun proteomics. Nat Protoc. 2016;11(12):2301-19. Epub 20161027. doi: 10.1038/nprot.2016.136. PubMed PMID: 27809316.

58. San Antonio JD, Jacenko O, Fertala A, Orgel J. Collagen Structure-Function Mapping Informs Applications for Regenerative Medicine. Bioengineering (Basel). 2020;8(1). Epub 20201229. doi: 10.3390/bioengineering8010003. PubMed PMID: 33383610; PMCID: PMC7824244.

59. Sweeney SM, Orgel JP, Fertala A, McAuliffe JD, Turner KR, Di Lullo GA, Chen S, Antipova O, Perumal S, Ala-Kokko L, Forlino A, Cabral WA, Barnes AM, Marini JC, San Antonio JD. Candidate cell and matrix interaction domains on the collagen fibril, the predominant protein of vertebrates. J Biol Chem. 2008;283(30):21187-97. Epub 20080515. doi: 10.1074/jbc.M709319200. PubMed PMID: 18487200; PMCID: PMC2475701.

60. Di Martino A, Cescon M, D'Agostino C, Schilardi F, Sabatelli P, Merlini L, Faldini C. Collagen VI in the Musculoskeletal System. Int J Mol Sci. 2023;24(6). Epub 20230307. doi: 10.3390/ijms24065095. PubMed PMID: 36982167; PMCID: PMC10049728.

61. Keene DR, Sakai LY, Burgeson RE. Human bone contains type III collagen, type VI collagen, and fibrillin: type III collagen is present on specific fibers that may mediate attachment of tendons, ligaments, and periosteum to calcified bone cortex. J Histochem Cytochem. 1991;39(1):59-69. doi: 10.1177/39.1.1983874. PubMed PMID: 1983874.

62. Williams L, Layton T, Yang N, Feldmann M, Nanchahal J. Collagen VI as a driver and disease biomarker in human fibrosis. FEBS J. 2022;289(13):3603-29. Epub 20210614. doi: 10.1111/febs.16039. PubMed PMID: 34109754.

63. Vandenbosch M, Nauta SP, Svirkova A, Poeze M, Heeren RMA, Siegel TP, Cuypers E, Marchetti-Deschmann M. Sample preparation of bone tissue for MALDI-MSI for forensic and (pre)clinical applications. Analytical and Bioanalytical Chemistry. 2021;413(10):2683-94. doi: 10.1007/s00216-020-02920-1. PubMed PMID: WOS:000569549100001.

64. Serowoky MA, Patel DD, Hsieh JW, Mariani FV. The use of commercially available adhesive tapes to preserve cartilage and bone tissue integrity during cryosectioning. Biotechniques. 2018;65(4):191-6. doi: 10.2144/btn-2018-0021. PubMed PMID: 30284932; PMCID: PMC6642614.

65. Khatib-Shahidi S, Andersson M, Herman JL, Gillespie TA, Caprioli RM. Direct molecular analysis of whole-body animal tissue sections by imaging MALDI mass spectrometry. Anal Chem. 2006;78(18):6448-56. doi: 10.1021/ac060788p. PubMed PMID: 16970320.

66. Bender KJ, Wang Y, Zhai CY, Saenz Z, Wang A, Neumann EK. Sample Preparation Method for MALDI Mass Spectrometry Imaging of Fresh-Frozen Spines. Anal Chem. 2023;95(47):17337-46. Epub 20231027. doi: 10.1021/acs.analchem.3c03672. PubMed PMID: 37886878; PMCID: PMC10688227.

67. Bellis SL. Advantages of RGD peptides for directing cell association with biomaterials. Biomaterials. 2011;32(18):4205-10. doi: 10.1016/j.biomaterials.2011.02.029. PubMed PMID: 21515168; PMCID: PMC3091033.

68. Bachmann MF, Oxenius A. Interleukin 2: from immunostimulation to immunoregulation and back again. EMBO Rep. 2007;8(12):1142-8. doi: 10.1038/sj.embor.7401099. PubMed PMID: 18059313; PMCID: PMC2267244.

69. Sondag CM, Combs CK. Adhesion of monocytes to type I collagen stimulates an APP-dependent proinflammatory signaling response and release of Aβ1-40. J Neuroinflamm. 2010;7. doi: Artn 22. 10.1186/1742-2094-7-22. PubMed PMID: WOS:000276405300001.

70. George A, Hao J. Role of phosphophoryn in dentin mineralization. Cells Tissues Organs. 2005;181(3-4):232-40. doi: 10.1159/000091384. PubMed PMID: 16612088.

71. Rappu P, Salo AM, Myllyharju J, Heino J. Role of prolyl hydroxylation in the molecular interactions of collagens. Essays Biochem. 2019;63(3):325-35. Epub 20190913. doi: 10.1042/EBC20180053. PubMed PMID: 31350381; PMCID: PMC6744578.

72. Garnero P. The contribution of collagen crosslinks to bone strength. Bonekey Rep. 2012;1:182. Epub 20120919. doi: 10.1038/bonekey.2012.182. PubMed PMID: 24363926; PMCID: PMC3868729.

73. Grzesik WJ, Frazier CR, Shapiro JR, Sponseller PD, Robey PG, Fedarko NS. Age-related changes in human bone proteoglycan structure. Impact of osteogenesis imperfecta. J Biol Chem. 2002;277(46):43638-47. Epub 20020906. doi: 10.1074/jbc.M202124200. PubMed PMID: 12221073.

74. Chang SH, Mori D, Kobayashi H, Mori Y, Nakamoto H, Okada K, Taniguchi Y, Sugita S, Yano F, Chung UI, Kim-Kaneyama JR, Yanagita M, Economides A, Canalis E, Chen D, Tanaka S, Saito T. Excessive mechanical loading promotes osteoarthritis through the gremlin-1-NF-kappaB pathway. Nat Commun. 2019;10(1):1442. Epub 20190329. doi: 10.1038/s41467-019-09491-5. PubMed PMID: 30926814; PMCID: PMC6441020.

75. Hosseininia S, Weis MA, Rai J, Kim L, Funk S, Dahlberg LE, Eyre DR. Evidence for enhanced collagen type III deposition focally in the territorial matrix of osteoarthritic hip articular cartilage. Osteoarthritis Cartilage. 2016;24(6):1029-35. Epub 20160111. doi: 10.1016/j.joca.2016.01.001. PubMed PMID: 26790721; PMCID: PMC4896400.

76. Volk SW, Shah SR, Cohen AJ, Wang Y, Brisson BK, Vogel LK, Hankenson KD, Adams SL. Type III collagen regulates osteoblastogenesis and the quantity of trabecular bone. Calcif Tissue Int. 2014;94(6):621-31. Epub 20140314. doi: 10.1007/s00223-014-9843-x. PubMed PMID: 24626604; PMCID: PMC4335719.

77. Chiba K, Ito M, Osaki M, Uetani M, Shindo H. In vivo structural analysis of subchondral trabecular bone in osteoarthritis of the hip using multi-detector row CT. Osteoarthritis Cartilage. 2011;19(2):180-5. Epub 20101116. doi: 10.1016/j.joca.2010.11.002. PubMed PMID: 21087677.

78. Komori T, Ji Y, Pham H, Jani P, Kilts TM, Kram V, Li L, Young MF. Type VI Collagen Regulates Endochondral Ossification in the Temporomandibular Joint. JBMR Plus. 2022;6(5):e10617. Epub 20220310. doi: 10.1002/jbm4.10617. PubMed PMID: 35509631; PMCID: PMC9059467.

79. Quarto R, Dozin B, Bonaldo P, Cancedda R, Colombatti A. Type VI collagen expression is upregulated in the early events of chondrocyte differentiation. Development. 1993;117(1):245-51. doi: 10.1242/dev.117.1.245. PubMed PMID: 8223249.

80. Pullig O, Weseloh G, Swoboda B. Expression of type VI collagen in normal and osteoarthritic human cartilage. Osteoarthritis Cartilage. 1999;7(2):191-202. doi: 10.1053/joca.1998.0208. PubMed PMID: 10222218.

81. Bailey KN, Nguyen J, Yee CS, Dole NS, Dang A, Alliston T. Mechanosensitive Control of Articular Cartilage and Subchondral Bone Homeostasis in Mice Requires Osteocytic Transforming Growth Factor beta Signaling. Arthritis Rheumatol. 2021;73(3):414-25. Epub 20210201. doi: 10.1002/art.41548. PubMed PMID: 33022131; PMCID: PMC9026749.

82. Meier F, Brunner AD, Koch S, Koch H, Lubeck M, Krause M, Goedecke N, Decker J, Kosinski T, Park MA, Bache N, Hoerning O, Cox J, Rather O, Mann M. Online Parallel Accumulation-Serial Fragmentation (PASEF) with a Novel Trapped Ion Mobility Mass Spectrometer. Mol Cell Proteomics. 2018;17(12):2534-45. Epub 20181101. doi: 10.1074/mcp.TIR118.000900. PubMed PMID: 30385480; PMCID: PMC6283298.

83. MacLean BX, Pratt BS, Egertson JD, MacCoss MJ, Smith RD, Baker ES. Using Skyline to Analyze Data-Containing Liquid Chromatography, Ion Mobility Spectrometry, and Mass Spectrometry Dimensions. J Am Soc Mass Spectrom. 2018;29(11):2182-8. Epub 20180725. doi: 10.1007/s13361-018-2028-5. PubMed PMID: 30047074; PMCID: PMC6191345.

84. Trede D, Schiffler S, Becker M, Wirtz S, Steinhorst K, Strehlow J, Aichler M, Kobarg JH, Oetjen J, Dyatlov A, Heldmann S, Walch A, Thiele H, Maass P, Alexandrov T. Exploring three-dimensional matrix-assisted laser desorption/ionization imaging mass spectrometry data: three-dimensional spatial segmentation of mouse kidney. Anal Chem. 2012;84(14):6079-87. Epub 20120705. doi: 10.1021/ac300673y. PubMed PMID: 22720760.

85. Zou KH, O'Malley AJ, Mauri L. Receiver-operating characteristic analysis for evaluating diagnostic tests and predictive models. Circulation. 2007;115(5):654-7. doi: 10.1161/CIRCULATIONAHA.105.594929. PubMed PMID: 17283280.

86. Klein O, Strohschein K, Nebrich G, Oetjen J, Trede D, Thiele H, Alexandrov T, Giavalisco P, Duda GN, von Roth P, Geissler S, Klose J, Winkler T. MALDI imaging mass spectrometry: discrimination of pathophysiological regions in traumatized skeletal muscle by characteristic peptide signatures. Proteomics. 2014;14(20):2249-60. Epub 20140821. doi: 10.1002/pmic.201400088. PubMed PMID: 25056804.

87. Xia J, Psychogios N, Young N, Wishart DS. MetaboAnalyst: a web server for metabolomic data analysis and interpretation. Nucleic Acids Res. 2009;37(Web Server issue):W652-60. Epub 20090508. doi: 10.1093/nar/gkp356. PubMed PMID: 19429898; PMCID: PMC2703878.

Figure Captions

Figure 1: Arthritis of the Tibial Plateau and Spatial Proteomic Imaging. (A) Non-arthritic Cadaveric Joint (control) cadaveric tissue donors without diagnosed arthritis, osteoporosis, or fracture, and Osteoarthritis (OA) patients receiving knee replacement compose a cohort that is age, sex, and BMI matched and stratified by their clinical OARSI (arthritis) grade. Safranin-O/Fast Green histologic staining (B) of the tibial plateau of a non-arthritic donor (Control - top) and a representative patient with Osteoarthritis (OA - bottom) depict the loss of proteoglycan staining (red) in Medial OA, indicative of cartilage loss. Separation of tissue into medial and lateral sections allows for both site-matched comparisons with cadaveric tissue (medial OA vs Medial Control, blue arrow) and tissue-matched comparisons to healthier tissue from the same OA patients (OA Medial vs OA Lateral, red arrow). Formalin-fixed, paraffin-embedded (FFPE) tissue sections are prepared (C) for MALDI-MSI spatial proteomics including deparaffinization and epitope retrieval prior to PNGase F enzyme treatment for removal of proteoglycans. Tissues are matrix-coated and imaged for glycomics before being washed and prepared for peptide imaging following a similar protocol utilizing collagenase III that targets the skeletal ECM. Following matrix application, slides are imaged (D) with the timsTOF fleX mass spectrometer (Bruker).

Figure 2: MALDI-MSI Identifies Molecular Features that Define the Skeletal ECM. Isolation of specific m/z features from the composite spectrum (A) of all imaged pixels allows for the generation of spatially resolved heatmaps of peptide distribution. Many peaks in the composite spectrum, of over 3,000 individual peaks, correspond to peptide ions preferentially found in bone or cartilage regions, others are detected across both tissues. We used the top 500 most abundant peaks from the composite spectrum to perform automated region segmentation (B) using a Bisecting K-means method with the SCiLS software. The number of automatically generated hierarchical segments (C) created was set to the minimal number needed to isolate the trabecular bone from the marrow space. Peptides of skeletal marker proteins (D) COL1A1, for bone, and COL2A1, for cartilage, are preferentially detected in the identified bone and cartilage areas (indicated in bold in spectrum Fig. 2A) demonstrating the agreement between the automatically generated regions and known skeletal tissues. *$p < 0.05$ of average pixel intensity in bone (orange) vs cartilage (blue). (E) High resolution scanning (20 μm step) in a tissue region composed of the bone and cartilage junction shows the clear spatial delineation of tissue type and spatial distribution of peptides within trabecular bone.

Figure 3: Site-matched Comparison, OA vs CAD Medial - Candidate Selection and Cohort Validation. Tissue sections of medial OA patients were compared against site-matched tissues from control cadaveric donors (A). The top 500 m/z features from the combined datasets were used to automatically generate tissue regions (B) that accurately segmented cartilage from bone and also identified 3 subtypes of bone including a region in the area of exposed subchondral bone (red, diseased bone). A pairwise comparison (C) between the non-arthritic subregion (orange) and the diseased region displayed many independent features with a higher intensity compared to the non-arthritic region, with fewer peaks elevated in the non-arthritic region. ROC analysis identified 31 peaks (D) that described the difference between the two isolated regions whose area under the predictive ROC curve was ≥0.85. (E) Several candidate features isolated from the representative pairwise analysis maintain significant difference between Cadaveric Medial (control) and OA Medial tissue sections within the full patient cohort in t-tests (n=4 per group). Examples of elevated markers by average pixel intensity from within the diseased tissue regions include peptides from COL1A1 and COL3A1 at 900.40 m/z and 1626.75 m/z respectively. *$p < 0.05$, (n=4).

Figure 4: Tissue-matched Comparison, OA Medial vs OA Lateral. Safranin-O staining of a representative arthritic tibial plateau shows the loss of cartilage (red) in the medial joint and robust cartilage staining in the lateral joint (A). OA joints were separated into medial and lateral halves from the same patient P1 for independent processing and imaging and combined into a single SCiLS Lab instance (B). The top 500 m/z features from both medial and lateral OA joints were used to automatically segment tissue regions (C) which accurately separated cartilage from bone (blue), identified sclerotic bone under areas of lost cartilage (red), and classified an additional transitional subtype of bone (yellow,) and a region of non-arthritic bone (orange). Pairwise comparison (D) between the automatically generated subregions of the non-arthritic and diseased regions identified 35 candidate features with AUC ≥0.85 (E). Guided manual segmentation (F) around the diseased regions of subchondral bone to the edge of exposed cartilage on the medial side compared to the intact subchondral bone of the lateral joint increased the predictive power of ROC analysis. The AUC for this peptide of COL1A1, GPAGERGEQ, at m/z = 900.40 increased from AUC = 0.850 to 0.951 with guided segmentation aided by both histology and the automated segmentation performed within SCiLS Lab.

Figure 5: Candidate Ion validation Across Multiple OA Patients Comparing Medial to Lateral Joints. (A) ROI's (green) were manually segmented around the outer most regions of the medial and lateral tibial plateaus of OA patients (n=4), using the edge of the cartilage layer (blue) as a guide for affected tissue in medial joints and using an equivalent distance on the lateral side. Average pixel

intensity within the segmented region was calculated for each candidate ion identified using automated tissue segmentation and ROC curve predictive score gating for both site and tissue matched comparisons. Visualization of data grouping by 3-dimensional PLS-DA (B) of pixel intensity showed distinct separation in the two joint sides despite complexity and patient heterogeneity in the OA medial cohort. Group-wide heat maps of candidate feature distribution (C) with peptide ID's belonging to several ECM component proteins, including several collagens and a member of the cartilage ECM, Asporin, depicted increases of the ion intensity in the outermost region of medial OA joints compared to their lateral counterparts. Statistical difference in feature intensity was confirmed via paired t-test $*p < 0.05$, (n=4 for each condition).

Figure 6: Visualizing the Post-translational Modification of Collagen in OA Bone. Heatmap of a peptide belonging to COL1A1, $I^{954}AGQRGVVGLP^{(ox)964}$, at 1082.63 m/z identified with a single hydroxyproline modification site at P^{964} (A), imaged at 20 µm laser step size from osteoarthritic human tibial plateau (knee) FFPE tissue. Replacement of the modified hydroxyproline with an unmodified proline resulted in the peptide $I^{954}AGQRGVVGLP^{964}$ with a m/z of 1066.64, a feature with very little detectable signal. (B) Heatmap of another COL1A1 peptide, $G^{656}KP^{(ox)}GEQGVP^{(ox)}GDLGAP^{(ox)670}$, identified at 1426.68 m/z with three hydroxyproline sites imaged at 20 µm laser step size. Replacement of the center hydroxyproline at P^{664} with an unmodified proline shifted the m/z by 15.994 Daltons, to a fainter peak at 1410.68 m/z representing the peptide $G^{656}KP^{(ox)}GEQGVPGDLGAP^{(ox)670}$ whose distribution resembled that of the triple-modified peptide. Continued replacement of prolyl hydroxylations to model the peptides with one or no modified prolines continued to shift the m/z and generated spatial maps with higher signal to noise that did not resemble the spatial distributions found for the peptides with a higher number of modifications.

Supplemental Figure 1: Clinical OA Tissues and Controls. Unstained tissue scans (A) and Safranin-O Histologic staining of FFPE slides of medial and lateral halves of the Tibial Plateau of Total Knee Arthroplasty (TKA) Patients and the lateral half from donor cadaveric non-arthritic Controls.

Supplemental Figure 2: Clinical Cohort Demographics. Tibial Plateaus from four 65-74 yr. old male subjects with clinically diagnosed stage IV Osteoarthritis (OA) receiving total knee replacement were recruited through referral from orthopedic surgeons at a Department of Veterans Affairs Medical Center, San Francisco. Fresh control cadaveric tissues (n=4) were obtained through the Willed Body Program at University of California, San Francisco from age, sex, and BMI matched donors without history of OA, osteonecrosis, osteoporosis, or fractures. * $p < 0.05$ by student's t-test showing that the control and OA patient cohorts can be distinguished by the OARSI grade (A) but are both BMI (B) and age (C) matched.

Supplemental Figure 3: Glycan Imaging. Imaging for glycan species was performed on a subset of 3 patient samples after PNGaseF treatment before application of collagenase enzyme. From a library of 165 known glycan species 46 glycan species were detected in human tibial plateau samples. In a limited OA cohort, lateral and medial tissue sections do not separate in a PCA analysis based on the mean glycan abundance per species per sample (A). Hierarchical clustering of the 46 detected species (B) shows variation in abundance of individual glycans across the small sample cohort resulting in no significant differences for glycans when comparing lateral and medial OA tissues in our small cohort (n=3). This comparison may be underpowered to detect specific OA related regulation on the glycan level. However, glycans with greater abundance in cartilage (C) or bone (D) regions were seen among the 46 detected species delineating cartilage and bone tissues, but these did not appear to be OA or damage regulated. Glycan imaging was also of high enough quality to accurately visualize small morphologic structures such as subchondral bone trabecula (E).

Supplemental Figure 4: Additional Spatial Markers by MALDI-MSI of Skeletal Tissue. Additional peptides of skeletal marker proteins COL1A1, $G^{626}PAGERGEQ^{634}$ at m/z 900.40, for bone, and COL2A1, $G^{998}PSGEPGKQGAP^{1010}$, for cartilage at m/z 1097.53 (A), are preferentially detected in the identified bone and cartilage areas demonstrating the agreement between the automatically generated regions and known skeletal tissues. *$p < 0.05$ of average pixel intensity in bone (orange) vs cartilage (blue). (B) High resolution scanning (20 μm step) in a tissue region composed of the bone and cartilage junction shows the spatial delineation of tissue type and spatial distribution of peptides within trabecular bone, interestingly this peptide of COL2A1 shows faint signal within trabecula but is

most prominently contained with the cartilage region. High resolution (20 um step size) images of the subchondral bone / cartilage junction for unidentified peptide feature at (C) 1943.91 m/z, (D) 1406.71 m/z, and (E) 1242.58 m/z show additional unique spatial distributions for different features and 'hot spots' within the subchondral trabecular bone and with signal from the cartilage region.

Supplemental Figure 5: OA Medial vs Cadaveric Medial Comparison. Site-matched comparison of arthritic OA medial tibial plateaus to age and BMI matched non-arthritic cadaveric tibial plateaus (A). Outlined blue areas show the identified cartilage tissue in OA and Cadaveric tissue used to delineate the subchondral bone region (Green) used for analysis. Three-dimensional PLS-DA confirms group separation in multiple component dimensions (B).

Supplemental Figure 6: Gradient of Disease in Age-related Osteoarthritis. A) Heatmap for a peptide of COL1A1 upregulated in OA Medial tissue in age-matched Cadaveric control and patient-matched OA Lateral tissue sections at 1211.61 m/z. B) Quantification of normalized pixel intensity for the same peptide showing gradient of increase from Cadaveric Lateral to OA Medial tissue sections. All four samples are statistically different from one another by post-hoc Tukey testing after one-way ANOVA ($p<0.05$). C) PLS-DA based on candidate pixel intensity from all human subjects (N=4) for Cadaveric Medial vs OA Lateral image data. This suggests that the two control populations describe different conditions or disease states.

Supplemental Figure 7: Tissue Segmentation and candidate ion generation from additional OA Patients. OA Patient 3 (P3) (A) was used to generate candidate features. The top 500 most abundant m/z features were used to automatically generate tissue regions (B). Isolation of the tissue regions containing sclerotic diseased bone and non-arthritic region allowed for feature analysis that results in (C) 37 candidate ions (D) that describe the difference between the independent regions with an area of the Receiver Operating Curve (ROC) of > 0.85. Comparison (E) of the 37 specific ions identified from patient #3 shared 19 ions in common with candidates generated from those identified using representative patient #1.

Supplemental Figure 8: Tissue-matched OA Medial vs Lateral Candidate m/z Comparisons. 30 of 44 candidates are significantly elevated in OA across the patient cohort by paired one-sided t-test ($p< 0.05$). 8 additional markers nearly significant ($0.1 < p < 0.05$)

Supplemental Figure 9: **Site-matched OA Medial vs CAD Medial Candidate m/z Comparisons.** 7 of 44 candidates significantly elevated in OA across the patient cohort by one-sided t-test. ($p<0.05$) 10 additional markers trending towards significance ($0.1 < p < 0.05$).

Supplemental Figure 10: MS/MS Spectra for Modified Peptides. Data Dependent Acquisition (DDA) MS/MS spectra of ions corresponding to MALDI-IMS features from Figure 6 matching peptides with 1 or more modified hydroxyproline residues identified as belong to COL1A1. Fragment ions from each precursor confirm the existence of modified hydroxyproline residues. A singly modified peptide IAGQRGVVGLP$^{(ox)}$, (A) at 1082.63 m/z was detected with multiple y-ions containing the hydroxyproline residue from this precursor. MS/MS spectra for fragments of the peptide G^{656}KP$^{(ox)}$GEQGVP$^{(ox)}$GDLGAP$^{(ox)}$ at m/z 1426.68 containing 3 HYP residues (B) and the corresponding peptide GKP$^{(ox)}$GEQGVPGDLGAP$^{(ox)}$ at m/z 1426.68 containing 2 HYPs (C) differ in b- and y- ion m/z by 16 m/z (15.994) at b9/y7 corresponding to the difference of 1 HYP modification. Note that in (C) fragments b6 and y13++ share the same m/z in MS/MS scans.

Supplemental Figure 11: Post-translational modifications on collagen may be enriched in OA tissues. When comparing the diseased outermost regions of OA medial tissue to tissue matched lateral controls (A) PTMs were found enriched in OA bone. A heatmap for a peptide of COL1A1 identified with 3 hydroxyprolines, (B) GKP$^{(ox)}$GEQGVP$^{(ox)}$GDLGAP$^{(ox)}$ at 1426.38 m/z showed the increased intensity for this feature in the diseased medial OA tissues. Intensity for the feature at 1410.68 m/z (C), corresponding to the loss of one hydroxyproline had less intensity in heatmaps. The loss of two hydroxyproline residues (D) to 1394.68 m/z had less noticeable signal then the more modified peptides. The fully unmodified peptide (E) had yet even less detectable signal in MALDI MS images. Quantification of the intensity of the PTM series across the cohort demonstrated that the modified peptides were consistently significantly elevated in OA tissues, no matter the number of proline modifications. Interestingly, while all comparisons remain significantly different between lateral and medial groups, the separation and the significance level (p value) decreased with sequential replacement of the prolyl hydroxylations (F).

Supplemental Figure 12: Bioactive Regions on Collagen Type 1 Upregulated in OA. Collagen Fibril binding partners for peptide sequences upregulated in medial human Osteoarthritis. A) The COL1A1 peptide G^{1165}PRGRTGD^{1173} at m/z 1139.58 exists in a region of the mature collagen fibril with multiple binding partners including, Amyloid Precursor Protein, Interleukin 2, and Phosphophoryn. B) Another COL1A1 peptide upregulated in medial OA tissues, G^{626}PAGERGEQ^{634} overlaps a known glycation site and a proposed region for keratan sulfate interaction. Protein

sequences of the mature Collagen 1 triple helix are shown as GenBankTM, α1(I) accession #NP000079.2 and α2(I) NP_000080.2. Amino Acid positions noted are from UniProt P02452 CO1A1_HUMAN and P08123 CO1A2_HUMAN. Collagen fibril binding zones schematics adapted from "Antonio, J. D. S., Jacenko, O., Fertala, A. & Orgel, J. P. R. O. Collagen Structure-Function Mapping Informs Applications for Regenerative Medicine. *Bioeng* 8, 3 (2020)". [1]PHOS: Phosphophoryn binding site. [2]C-Pep. Domain - C-telopeptide fibrillogenesis nucleation domain. [3]KSPG: KSPG - Proposed sites of keratan sulfate proteoglycan binding.

Supplemental Figure 13: Larger Study Overlook. Future directions utilizing MALDI-MSI in OA on the protein level to explore and define OA are very promising. Knee tissues from Total Knee Arthroplasty (TKA) patients from larger OA sample populations, including specific cohorts of female donors, will be used in similar foundational studies to expand the number of possible peptide features/biomarkers for OA. These candidates will be identified via MALDI-MSI and validated via complementary MS/MS technologies in studies of OA models *in vitro* and *in vivo.* Validated peptide OA biomarkers could be used as potential diagnostic markers from synovial fluid or even circulating plasma to track OA risk and progression in a viable clinical method.

Supplemental Tables 1-4.

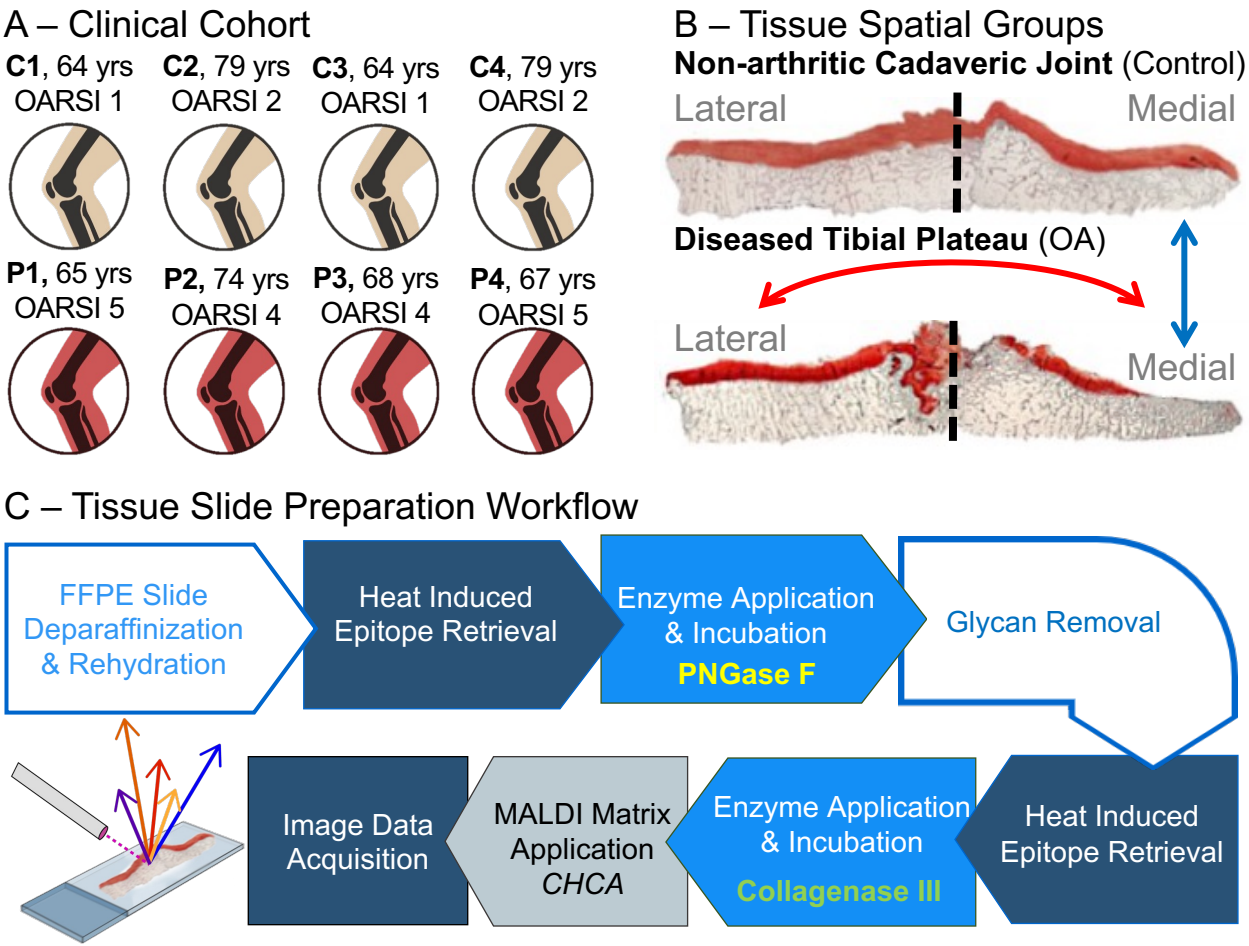
A – Clinical Cohort
C1, 64 yrs
OARSI 1
C2, 79 yrs
OARSI 2
C3, 64 yrs
OARSI 1
C4, 79 yrs
OARSI 2
P1, 65 yrs
OARSI 5
P2, 74 yrs
OARSI 4
P3, 68 yrs
OARSI 4
P4, 67 yrs
OARSI 5
B – Tissue Spatial Groups
Non-arthritic Cadaveric Joint (Control)
Lateral
Medial
Diseased Tibial Plateau (OA)
Lateral
Medial
C – Tissue Slide Preparation Workflow
FFPE Slide Deparaffinization & Rehydration
Heat Induced Epitope Retrieval
Enzyme Application & Incubation
PNGase F
Glycan Removal
Heat Induced Epitope Retrieval
Enzyme Application & Incubation
Collagenase III
MALDI Matrix Application
CHCA
Image Data Acquisition

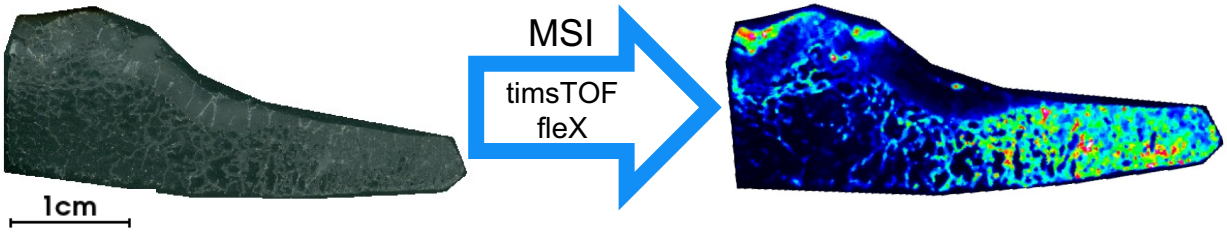
D - Molecular Imaging of Skeletal Tissue
1cm
MSI
timsTOF fleX

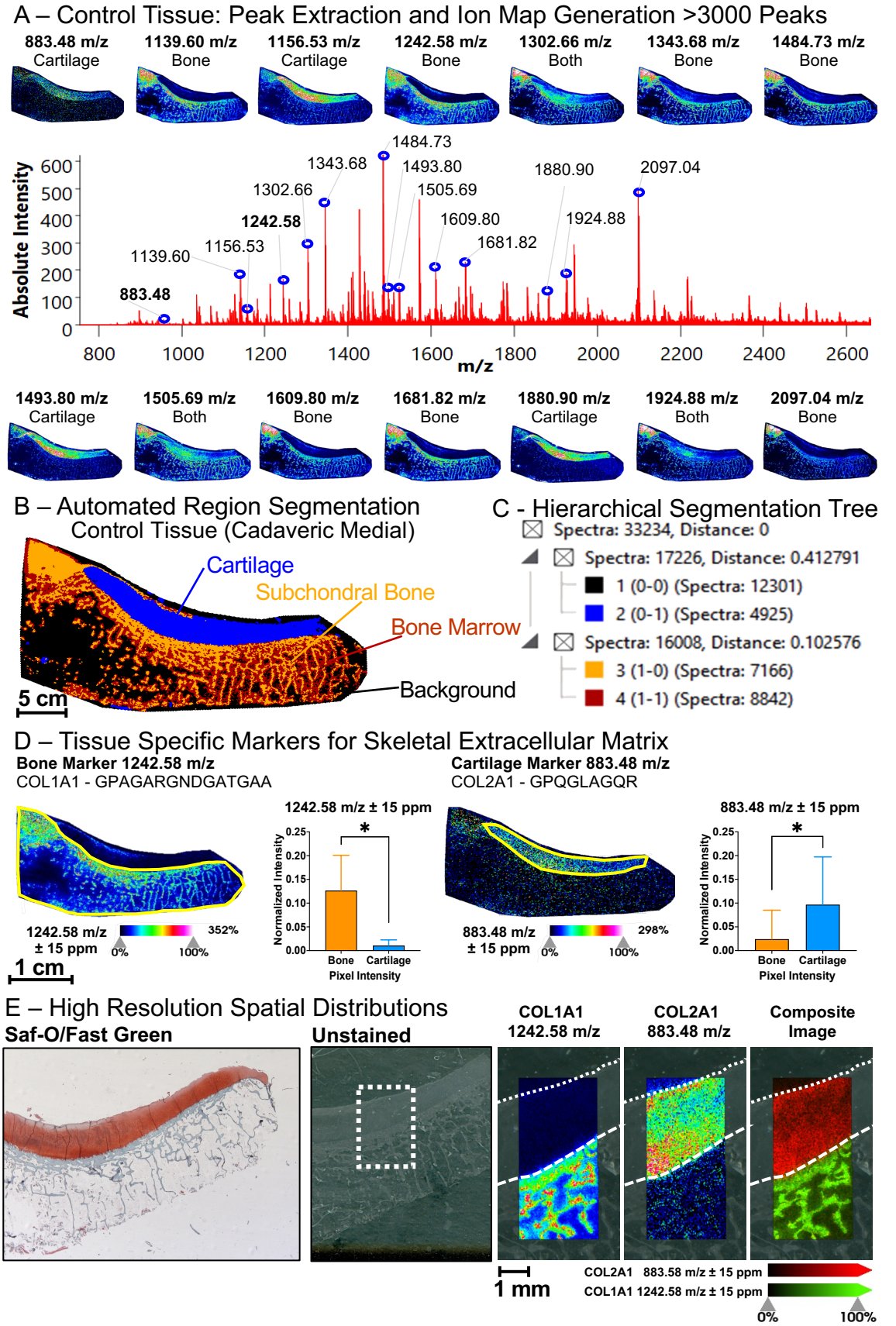
A – Control Tissue: Peak Extraction and Ion Map Generation >3000 Peaks
883.48 m/z Cartilage
1139.60 m/z Bone
1156.53 m/z Cartilage
1242.58 m/z Bone
1302.66 m/z Both
1343.68 m/z Bone
1484.73 m/z Bone
Absolute Intensity
m/z
1493.80 m/z Cartilage
1505.69 m/z Both
1609.80 m/z Bone
1681.82 m/z Bone
1880.90 m/z Cartilage
1924.88 m/z Both
2097.04 m/z Bone
B – Automated Region Segmentation
Control Tissue (Cadaveric Medial)
Cartilage
Subchondral Bone
Bone Marrow
Background
5 cm
C - Hierarchical Segmentation Tree
Spectra: 33234, Distance: 0
Spectra: 17226, Distance: 0.412791
1 (0-0) (Spectra: 12301)
2 (0-1) (Spectra: 4925)
Spectra: 16008, Distance: 0.102576
3 (1-0) (Spectra: 7166)
4 (1-1) (Spectra: 8842)
D – Tissue Specific Markers for Skeletal Extracellular Matrix
Bone Marker 1242.58 m/z
COL1A1 - GPAGARGNDGATGAA
Cartilage Marker 883.48 m/z
COL2A1 - GPQGLAGQR
1242.58 m/z ± 15 ppm
352%
0%
100%
1 cm
Normalized Intensity
Bone
Cartilage
Pixel Intensity
883.48 m/z ± 15 ppm
298%
E – High Resolution Spatial Distributions
Saf-O/Fast Green
Unstained
COL1A1 1242.58 m/z
COL2A1 883.48 m/z
Composite Image
1 mm
COL2A1 883.58 m/z ± 15 ppm
COL1A1 1242.58 m/z ± 15 ppm

A – Site Matched Comparison

Cadaveric (Control)

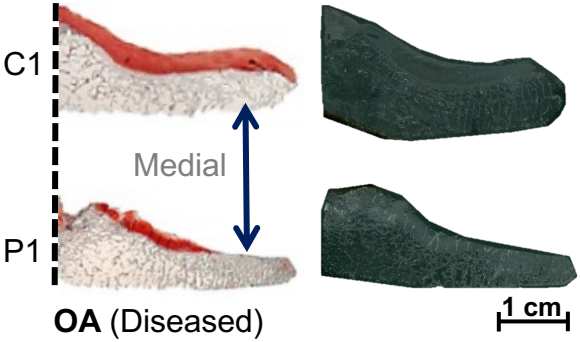

OA (Diseased)

B - Automated Region Segmentation

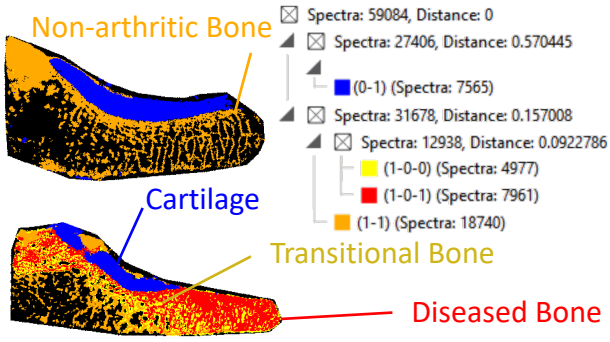

C – Subchondral Bone Region Comparison

Non-arthritic Bone vs Diseased Bone

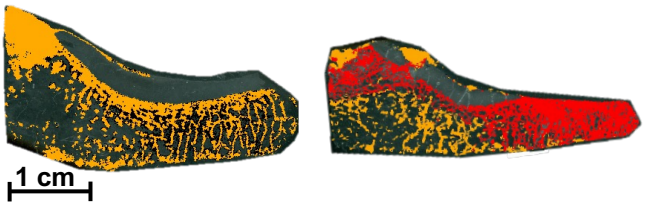

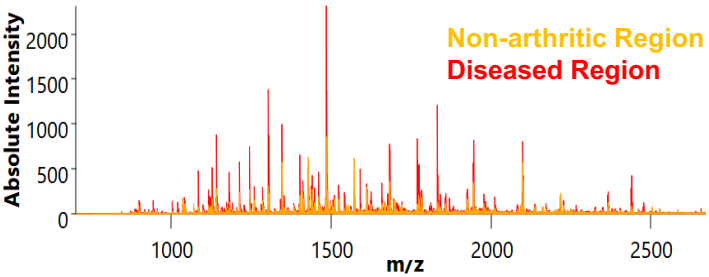

D – 31 Candidate Features, P1

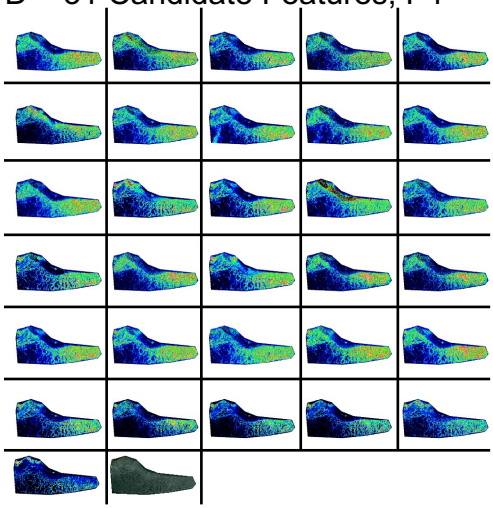

E - Ion Distribution Maps for Candidate Marker Peptides for OA

COL1A1 – GPAGERGEQ

CAD Medial OA Medial

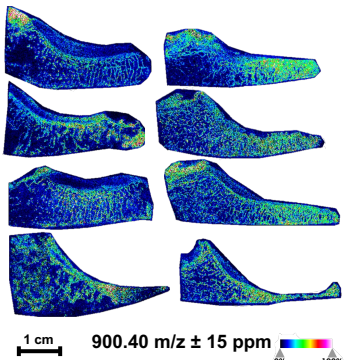

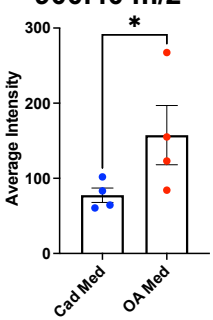

COL3A1 - GEP$^{(ox)}$GAN$^{(de)}$GLP$^{(ox)}$GAAGERGAP$^{(ox)}$

CAD Medial OA Medial

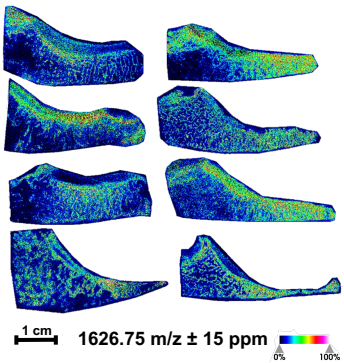

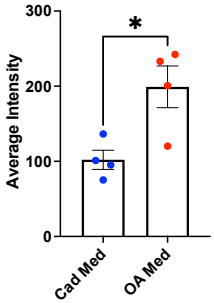

A – Tissue Match Comparison

Patient Matched Unstained Tibial Plateau Halves

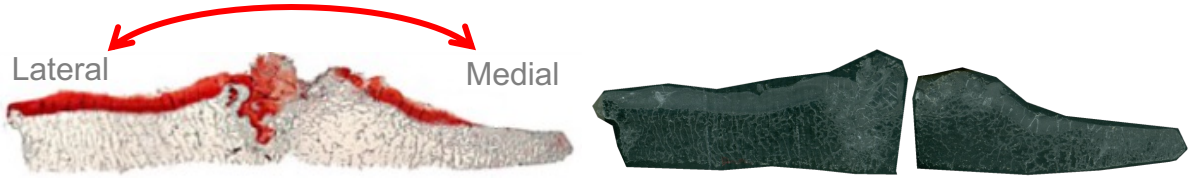

B - Automated Region Segmentation

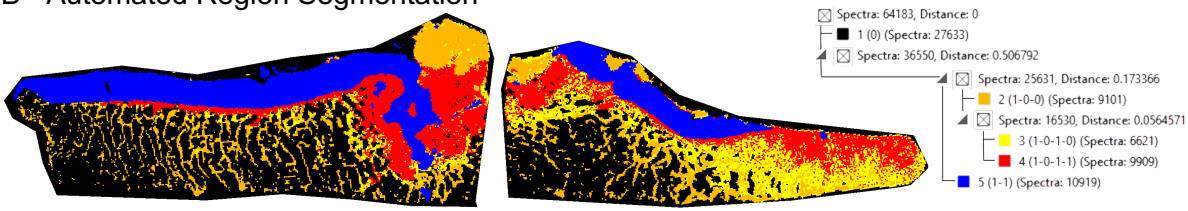

C – Subchondral Bone Region Comparison

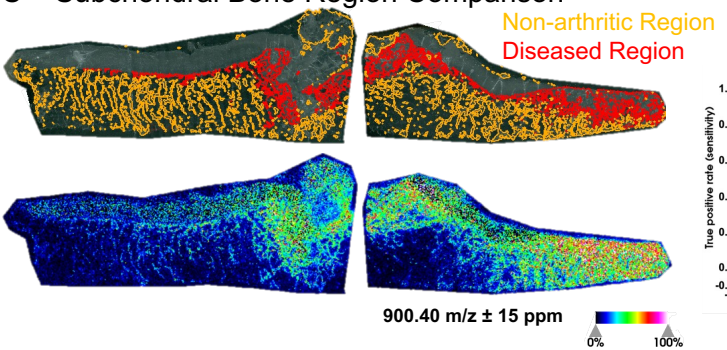

COL1A1 – GPAGERGEQ

AUC= 0.872, 900.40 m/z ± 15 ppm

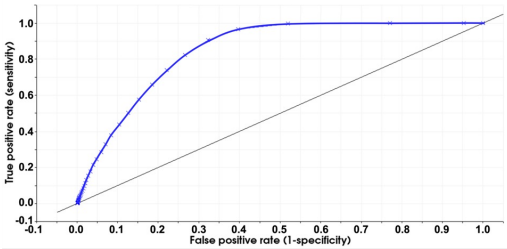

D – 34 candidate features with an AUC > 0.85 Non-arthritic Region vs Diseased Region

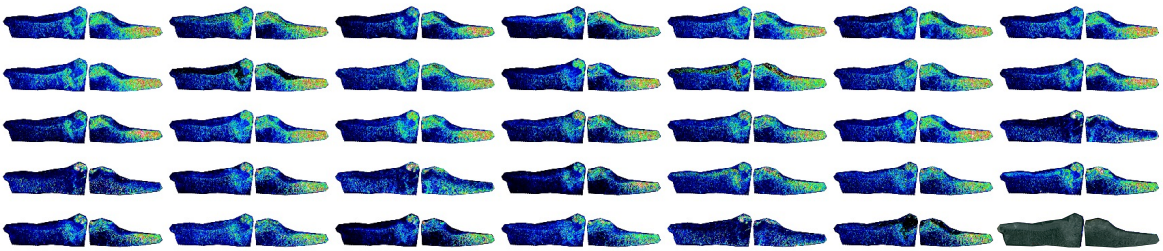

E - Guided Region Segmentation Around Damaged Tissues Increases Feature Separation

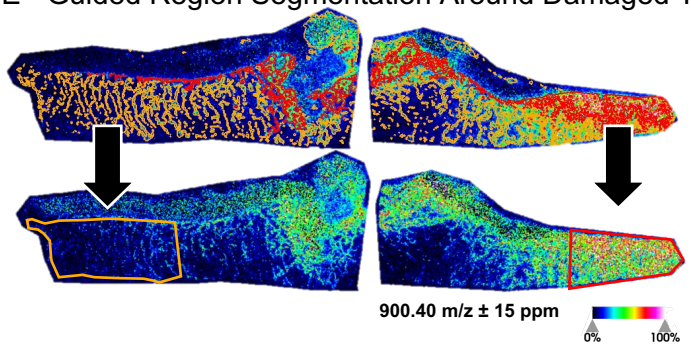

COL1A1 – GPAGERGEQ

AUC= 0.951, 900.40 m/z ± 15 ppm

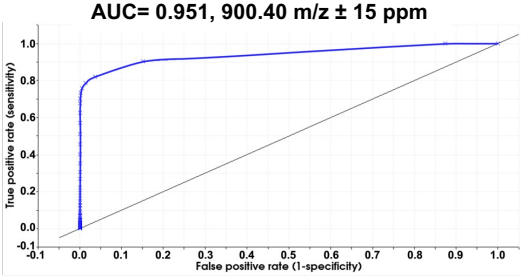

A – ROI Selection for Site Matched damaged subchondral bone

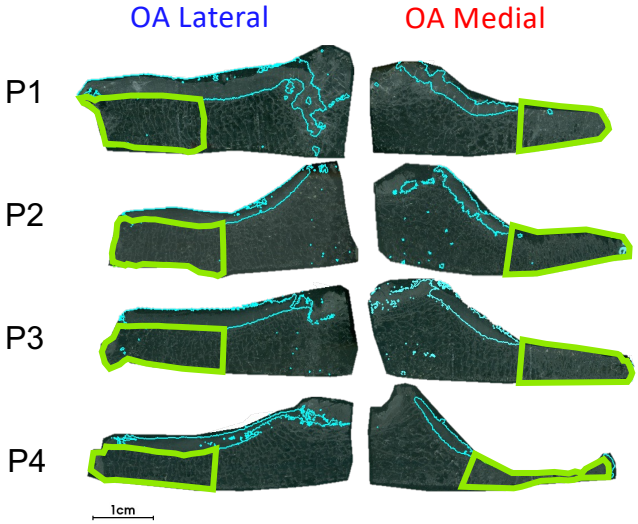

B – PLS-DA OA Med vs OA Lat

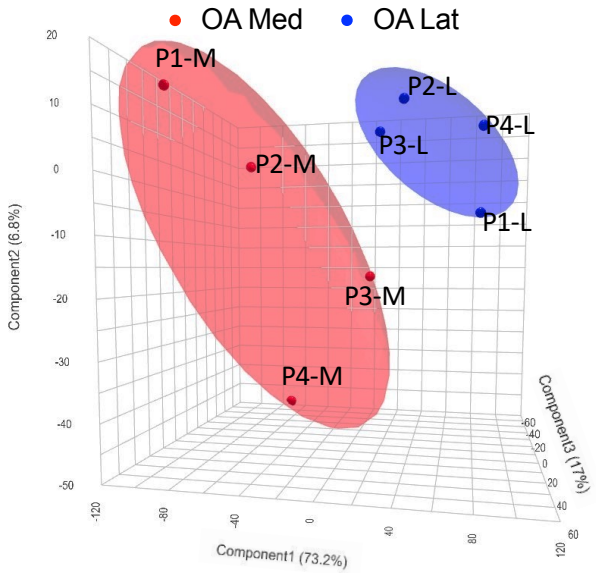

C - Ion Distribution Maps for Candidate Marker Peptides for OA

COL3A1 GQRGEP(ox)GPQ

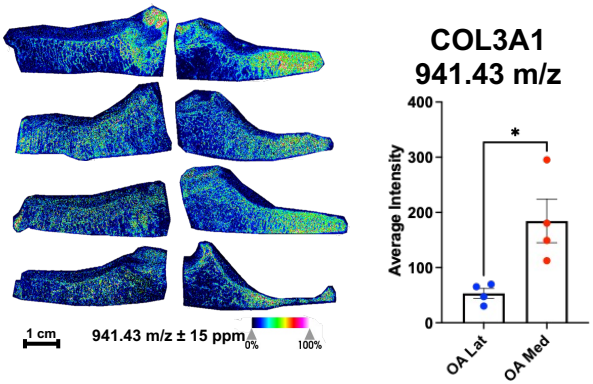

COL1A1 - GPRGRTGD

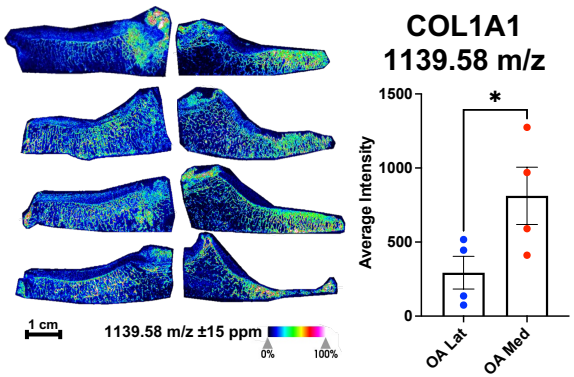

ASPN – ANPLDNN(de)GIEPGAFEG

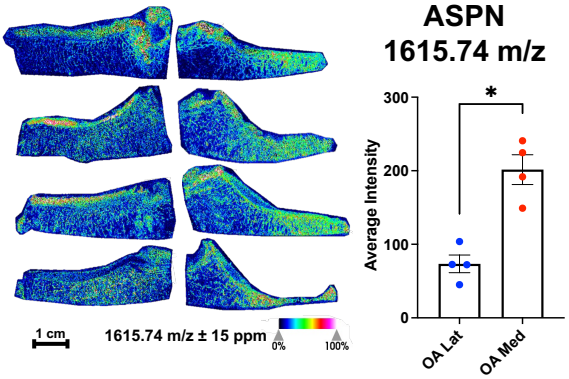

COL6A3 - GEIGLDGLDGEDGDKGLP(ox)

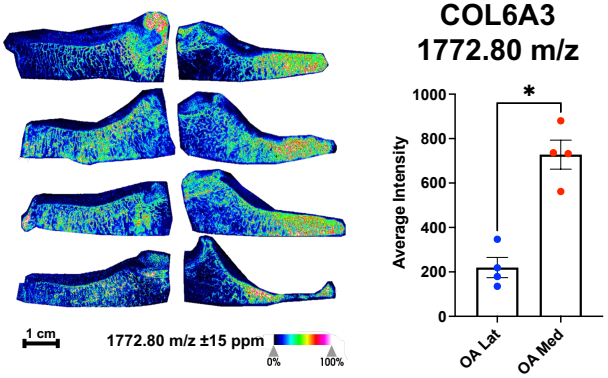

A – Visualizing Post-Translational Modifications of COL1A1 in OA Bone

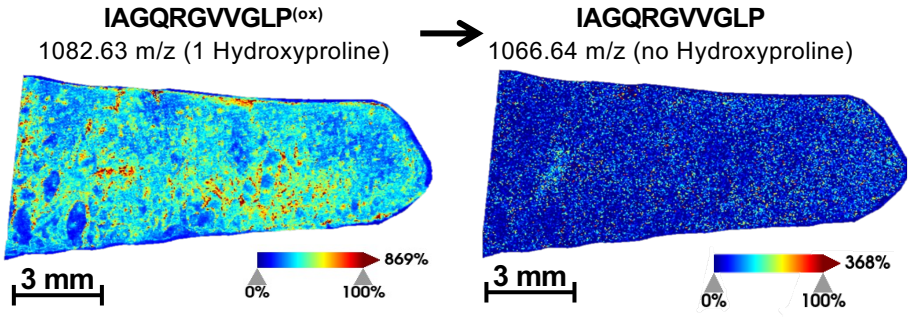
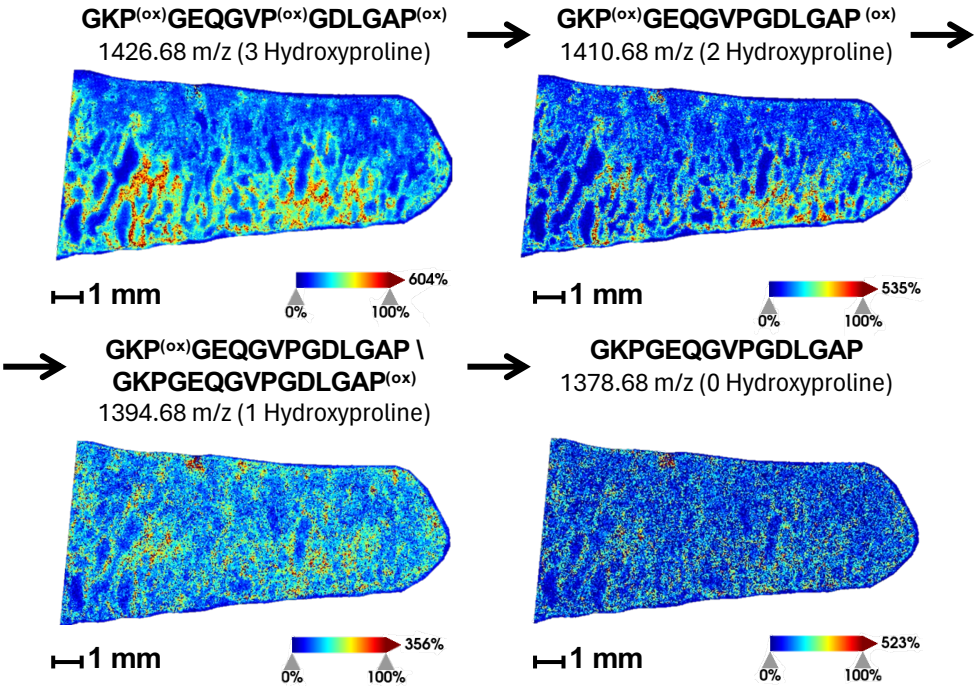
B – Sequential Loss of Hydroxyprolines from a Multiply-modified COL1A1 Peptide